GEORGIA DOT RESEARCH PROJECT 14-30
FINAL REPORT

Field Validation of a Drive-By Bridge Inspection System with Wireless BWIM + NDE Devices

Georgia Department of Transportation

OFFICE OF RESEARCH
15 KENNEDY DRIVE
FOREST PARK, GA 30297-2534

TECHNICAL REPORT STANDARD TITLE PAGE

1.Report No.: FHWA-GA-16-1430	2. Government Accession No.:	3. Recipient's Catalog No.:
4. Title and Subtitle: Field Validation of a Drive-By Bridge Inspection System with Wireless BWIM + NDE Devices		5. Report Date: September 2016
		6. Performing Organization Code:
7. Author(s): Yang Wang, Nasim Uddin, Laurence J. Jacobs, Jin-Yeon Kim		8. Performing Organ. Report No.:
9. Performing Organization Name and Address: School of Civil and Environmental Engineering Georgia Institute of Technology 790 Atlantic Dr NW Atlanta, GA 30332-0355		10. Work Unit No.:
		11. Contract or Grant No.: RP 14-30
12. Sponsoring Agency Name and Address: Georgia Department of Transportation Office of Research 15 Kennedy Drive Forest Park, GA 30297-2534		13. Type of Report and Period Covered: Final; January 2015 – September 2016
		14. Sponsoring Agency Code:
15. Supplementary Notes: Prepared in cooperation with the U.S. Department of Transportation, Federal Highway Administration.		

16. Abstract:

In this project, researchers developed and performed field validation of a wireless structural sensing system for a variety of bridge response measurements, including strain, acceleration, and displacement. The research team used the wireless strain measurement for bridge weigh-in-motion (BWIM) analysis, correlating vibration data of the bridge with the axle loads of the test vehicle. A drive-by bridge inspection system, instrumented with wireless sensors, consisting of portable wireless BWIM+NDE devices was developed for providing automated and convenient bridge safety evaluation. It was integrated with state-of-the-art ultrasonic nondestructive evaluation (NDE) technologies that can assist in monitoring damage growth in critical structural members.

17. Key Words: wireless structural sensing, bridge monitoring, bridge weigh-in-motion, drive-by in section, nondestructive evaluation		18. Distribution Statement:	
19. Security Classification (of this report): Unclassified	20. Security Classification (of this page): Unclassified	21. Number of Pages: 62	22. Price:

Form DOT 1700.7 (8-69)

GDOT Research Project No. 14-30

Final Report

FIELD VALIDATION OF A DRIVE-BY BRIDGE INSPECTION SYSTEM WITH WIRELESS BWIM + NDE DEVICES

By

Yang Wang

Laurence J. Jacobs

Jin-Yeon Kim

School of Civil and Environmental Engineering
Georgia Institute of Technology

and

Nasim Uddin

Department of Civil, Construction, and Environmental Engineering
The University of Alabama at Birmingham

Contract with

Georgia Department of Transportation

In cooperation with

U.S. Department of Transportation
Federal Highway Administration

September 2016

Table of Contents

Page

List of Tables

List of Figures

Executive Summary

The expansion in highway freight shipments in recent years has led to a substantial increase in truck traffic. The use of heavy vehicles (i.e., 18 wheelers) has become the backbone of logistics and economic success, and national projections predict that freight shipments will double in the next ten years. Of particular concern are the increased number, size, and weight of heavy commercial vehicles, with some being illegally overloaded. Overloaded vehicles can endanger the safety of transportation infrastructure and cause expensive premature structural damage. As early as 1990, a *Truck Weight Limits* study by the Transportation Research Board (TRB) showed that illegally overweight trucks cost highway agencies $160 million to $670 million annually *on pavement*—damage to bridges was not included in that study. To this end, the bridge weigh-in-motion (BWIM) method uses existing bridges as weighing scales to identify the axles and gross weight of passing trucks.

With support from the Georgia Department of Transportation (GDOT), the researchers in this project have developed a rapidly deployable, low-cost, wireless sensing system with structural health monitoring capability. While the traditional cabled BWIM system costs ~$120,000 each, by removing lengthy cables and bulky equipment, this new wireless system provides a solution that significantly reduces cost. The main objectives of this project included:

1. Field validation of the wireless structural sensing system for a variety of bridge response measurements, including strain, acceleration, and displacement.
2. Usage of the wireless strain measurement for BWIM analysis, correlating vibration data of the bridge with the axle loads of the test vehicle.

3. Development of a drive-by bridge inspection system, instrumented with wireless sensors, consisting of portable wireless BWIM+NDE devices for providing automated and convenient bridge safety evaluation.
4. Integration with state-of-the-art ultrasonic nondestructive evaluation (NDE) technologies that can assist in monitoring damage growth in critical structural members.

Acknowledgements

The research reported herein was sponsored by the Georgia Department of Transportation through Research Project Number 14-30. Mr. Ralph (Trey) Daniell, Mr. Clayton Bennett, and Mr. Andy J. Doyle of the Georgia Department of Transportation provided invaluable guidance and technical information. Mr. David Jared and Mr. Yusuf Ahmed carefully oversaw the quarterly progress reports. The opinions and conclusions expressed herein are those of the authors and do not represent the opinions, conclusions, policies, standards, or specifications of the Georgia Department of Transportation or of other cooperating organizations.

1 Wireless Sensor Instrumentation on a Highway Bridge

This chapter presents the validation testing of a wireless sensing system the research team developed and installed on a highway bridge in Bartow County, Georgia. Section 1.1 introduces the testbed bridge. Section 1.2 describes the wireless sensing system that was instrumented. In Section 1.3, the performance of the developed wireless sensing system in the field testing is presented. Section 1.4 describes the modeling of the highway bridge and the finite element updating using the field test data.

1.1 Highway bridge introduction

The testbed bridge was built in 2006, and is located on Highway SR113 over Dry Creek in Bartow County, Georgia, USA. The bridge has two lanes carrying the eastbound traffic. FIGURE 1-1 shows the plan and elevation views of the entire bridge. The bridge consists of three skewed spans, which are 70 feet long each. The continuous reinforced concrete bridge deck is supported by five I-shaped pre-stressed concrete girders, denoted as G1 to G5 in FIGURE 1-1(a). The girders are spaced 8 feet 9 inches away from one another, connected by lateral diaphragms, and simply supported at the two ends of every span. The detailed support condition is shown in FIGURE 1-1(b), where EXP stands for expansion and FIX stands for fixed. The research team chose the west span among the three for instrumentation. FIGURE 1-2 shows the top and bottom views of the bridge. Overall, the researchers found the bridge to be in very good condition and to be a fitting testbed bridge for BWIM studies.

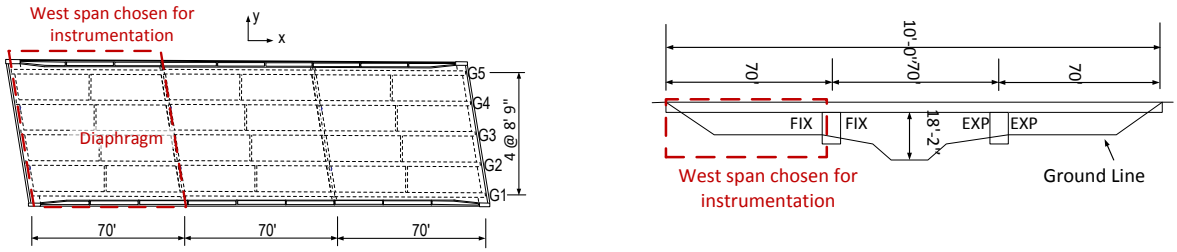

(a) (b)

FIGURE 1-1 SR113 bridge over Dry Creek: (a) plan view; (b) elevation view

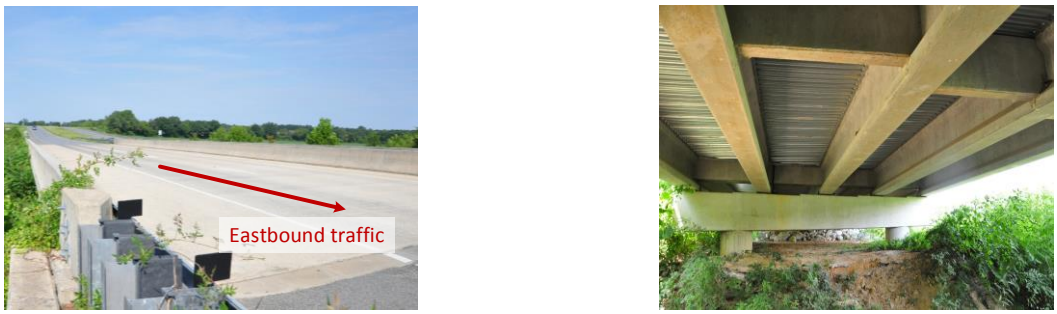

(a) (b)

FIGURE 1-2 Bridge photos: (a) top view; (b) bottom view

1.2 Instrumentation of the *Martlet* wireless sensing system

This section presents the instrumentation of the wireless sensing system for the field validation test. The *Martlet* wireless sensing system is briefly introduced, followed by a detailed description of the sensor installation plan on the highway bridge.

1.2.1 Martlet wireless sensing system

The wireless sensing system used in this test is named *Martlet* [1]. The *Martlet* wireless node uses a dual-core microcontroller (TMS320F28069) as the processer, featuring up to 90 MHz programmable clock frequency. The 9-channel 12-bit analog-to-digital converter (ADC) allows *Martlet* to sample analog sensor signals at a rate up to 3 MHz. For wireless communication, *Martlet* uses a 2.4-GHz low-power radio conforming to the IEEE 802.15.4 standard [2]. The extensible hardware design of *Martlet* allows easy

interfacing with various kinds of sensors by conveniently stacking the sensor boards on top of the *Martlet* motherboard. Furthermore, a microSD card up to 32 GB of memory can be inserted into *Martlet* for long-term data acquisition.

In this validation test, four types of sensors were interfaced with *Martlet* through corresponding sensor boards (termed "wing" boards). As shown in FIGURE 1-3(a), the integrated accelerometer wing board includes a low-cost microelectromechanical (MEMS) accelerometer and an on-board signal conditioning circuit that performs mean shifting, low-pass filtering, and amplification [3]. The use of digital potentiometers in the design makes the low-pass cutoff frequency and amplification gain of the integrated accelerometer wing remotely programmable. FIGURE 1-3(b) shows the strain gage wing board connected with a 90 mm strain gage for installation on the bridge girders. The strain gage wing board can be connected with 120 Ω or 350 Ω strain gages, providing selectable amplification gains at ×96 and ×477 and low-pass filtering at 25 Hz. FIGURE 1-3(c) shows the smart ADC/DAC wing board [1] connected with an MTS magnetostrictive (CS194AV) linear-position displacement sensor, which was used to measure the displacement of the girders. The ADC/DAC wing board powered the displacement sensor at 5 V and provided programmable amplification gain from ×1.9 to ×190 and on-board low-pass filtering from

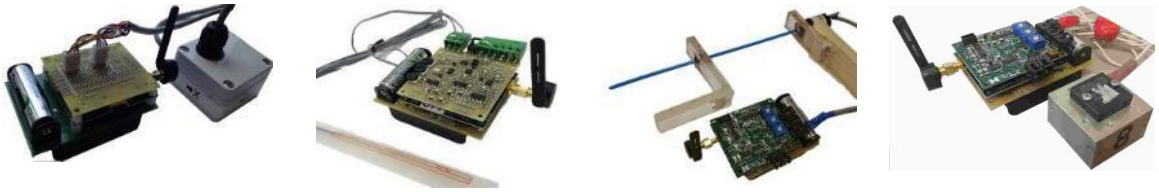

(a) (b) (c) (d)

FIGURE 1-3 Wireless sensing boards interfaced with *Martlet*: (a) integrated accelerometer board; (b) strain gage board; (c) smart ADC/DAC sensor board with a magnetostrictive displacement sensor; (d) smart ADC/DAC sensor board with an accelerometer

15 Hz to a few hundred Hz. As shown in FIGURE 1-3(d), the ADC/DAC wing can also be used to connect with a high-precision accelerometer, Silicon Designs 2012-002.

1.2.2 Instrumentation plan

Because of its low cost and versatility, the *Martlet* sensing system is able to incorporate various types of sensors to be installed on the bridge. To accurately capture the bridge vibrations, a total of 15 accelerometers, 12 strain gages, and 5 magnetostrictive displacement sensors were instrumented.

As shown in FIGURE 1-4(a), the accelerometers were instrumented on the bottom side of every girder, at quarter span and mid-span locations, to measure vertical

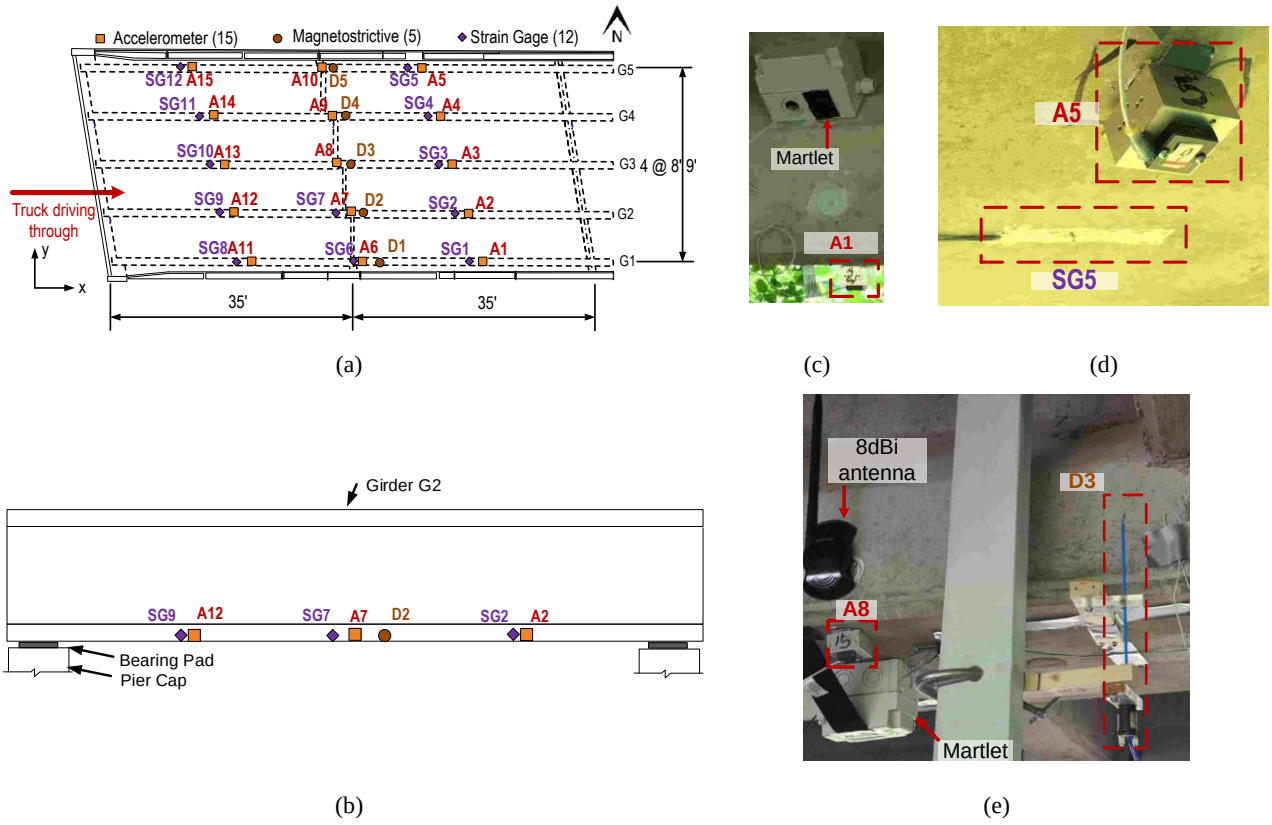

(a) (c) (d)

(b) (e)

FIGURE 1-4 Summary of instrumentation: (a) instrumentation plan; (b) elevation view of girder G2; (c) accelerometer A1; (d) accelerometer A5 and strain gage SG5; (e) displacement sensor D3 and accelerometer A8

accelerations. The strain gages were installed at similar locations to measure the longitudinal deformation. The five magnetostrictive displacement sensors were installed at the mid-span of every girder to measure the vertical displacement (FIGURE 1-4(b)). Furthermore, the corresponding *Martlet* wireless nodes were protected by weatherproof boxes and attached to the girders. FIGURE 1-4(c) through (e) show the close-up views of different types of sensors at several locations.

1.3 Field testing results

This section presents the results of the field validation tests. The vibration responses of the highway bridge when excited by a small truck and a large truck are presented first. In addition, the modal properties of the highway bridge extracted from an impact hammer test are given. Finally, based on the modal properties obtained from the field test, finite element (FE) model updating conducted to improve the accuracy of the FE model is provided.

1.3.1 Bridge vibration measurement

Bridge vibration responses were measured under different traffic excitations. For the results presented in this subsection, the amplification gain was set as ×20 for accelerometers, ×477 for the strain gages, and ×50 for the magnetostrictive displacement sensors. The cutoff frequency of the on-board low-pass filter was set at 25 Hz for all sensors. The sampling frequency was set as 200 Hz.

FIGURE 1-5 shows the comparison of the vibration responses for two different trucks. The plots include the bridge acceleration measurements from sensors A12 and A13, the strain measurements from SG9 and SG10, and the displacement measurements from

D2 and D3 (see FIGURE 1-4). Compared to responses from the small truck, the magnitudes of the bridge responses from the large truck clearly increased, as shown in all the acceleration, strain, and displacement plots. Overall, the traffic-induced vibration measurements demonstrate the reliability and versatility of the *Martlet* wireless sensing system, and thus, its potential for detecting truck weight.

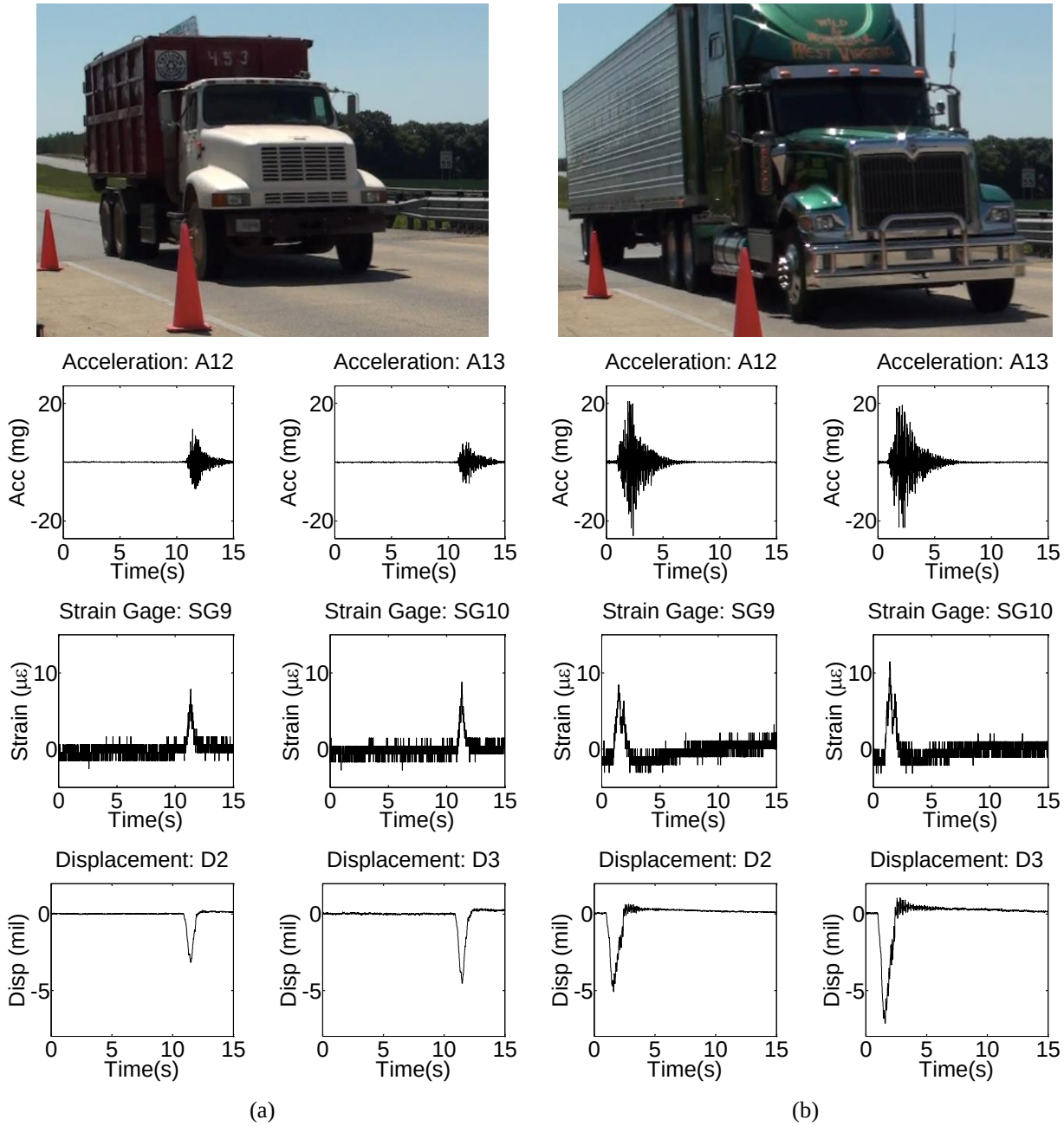

FIGURE 1-5 Bridge vibration measurement: (a) small truck; (b) large truck

1.3.2 Modal property analysis

To obtain modal vibration properties of the bridge, a 12.1-lb modal hammer with a hard plastic head (PCB Piezotronics 086D50) was used. Hammer impact was applied on the bridge deck at the 2/3 span of girder G1. The acceleration response was sampled at 1000 Hz for 15 seconds in total. FIGURE 1-6 shows the frequency spectra of all acceleration channels under hammer excitation. Four peaks are observed in the frequency spectra under 25 Hz, which correspond to the approximate values of the first four captured resonance frequencies.

To obtain detailed modal properties, the acceleration responses were analyzed to extract the resonance frequencies, damping ratios, and the corresponding mode shapes of

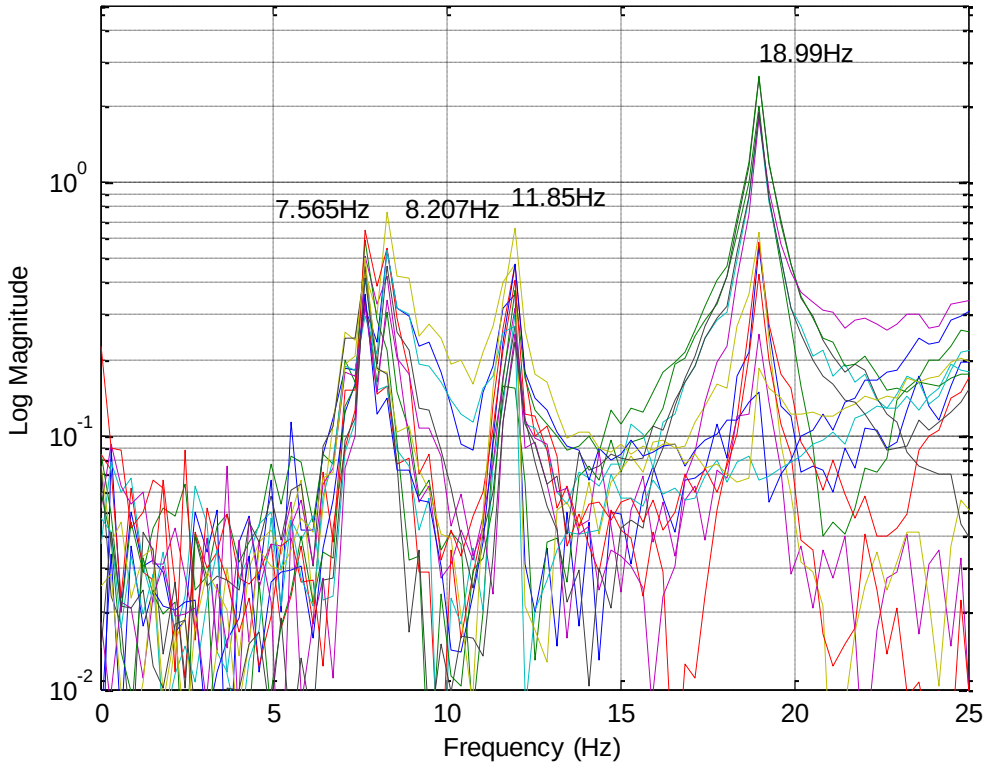

FIGURE 1-6 Frequency spectra of all acceleration channels in hammer test

the bridge. The commonly used eigensystem realization algorithm (ERA) [4] was adopted here and the first four modes were extracted (FIGURE 1-7). The resonance frequency of every mode matches well with the corresponding peak location in the frequency spectra. Specifically, Mode 1 shows all five girders bending in one direction, which is expected for this simply-supported bridge span. Mode 2 shows opposite bending directions between girders G1 and G2 and G4 and G5, while girder G3 moves relatively little. Mode 3 shows the opposite bending directions between side girders G1 and G5 and middle girders G2, G3, and G4. Mode 4 shows the alternating bending directions among girders G1, G2, G4, and G5. All the modes agree well with the typical behavior of a simply-supported bridge span.

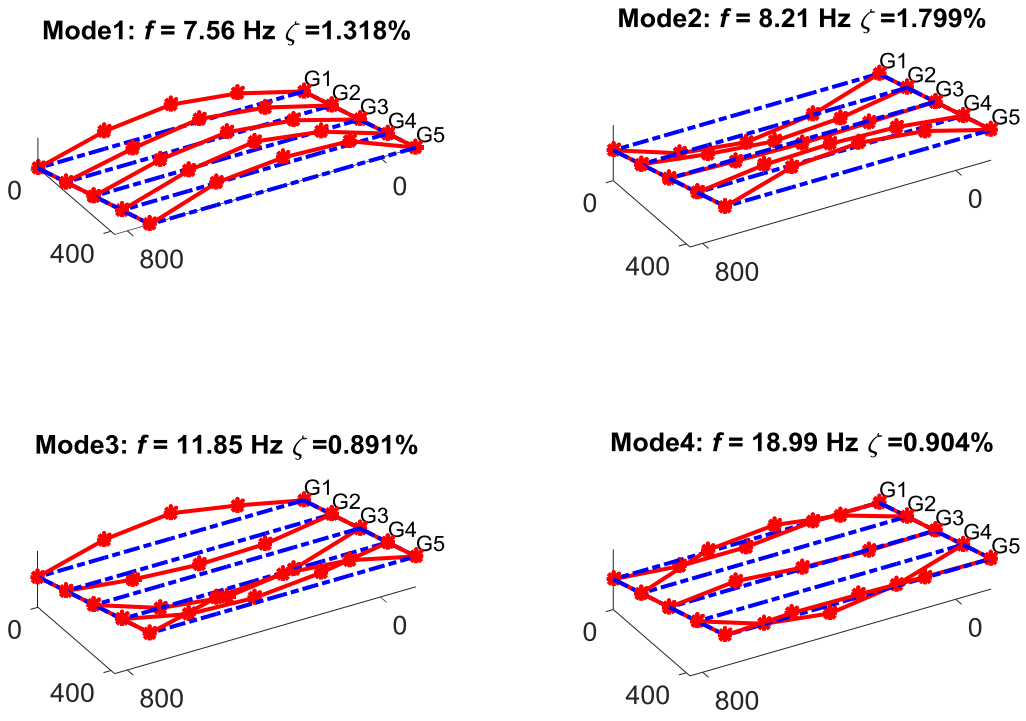

FIGURE 1-7 Resonance frequencies and mode shapes of the bridge span

1.4 Finite element modeling and model updating

An accurate finite element model of the bridge span is needed for bridge weigh-in-motion analysis. To this end, an initial FE model was first built based on design drawings and nominal material properties. Subsection 1.4.1 describes this model. In Subsection 1.4.2, modal properties obtained from Subsection 1.3.2 are used to update selected model parameters to obtain a more accurate FE model that provides the same vibration modal properties measured at the bridge.

1.4.1 Initial finite element modeling of the highway bridge

According to the drawing and field inspection, a three-dimensional FE model was built in a commercial software package, ANSYS. The FE model is shown in FIGURE 1-8. In the drawings, the x-axis represents the longitudinal (east) direction of the bridge span, the y-axis the transverse (north) direction, and the z-axis the vertical direction. The concrete deck was simulated using SHELL181 elements. Other components, including girders, pre-stressed strands, diaphragms, barriers, end beam, and end wall, were modeled using BEAM188 elements. Besides using BEAM188 elements to simulate the pre-stressed strands, the pre-stressed effect was simulated by assigning initial strain to the strands. Finally, proper boundary conditions were assigned to the model. As shown in FIGURE 1-9, the y and z directions were constrained at both sides of each girder. At the end wall side, translational springs were assigned along the x direction for both girders and the deck. TABLE 1-1 lists the initial values of the spring stiffness constants.

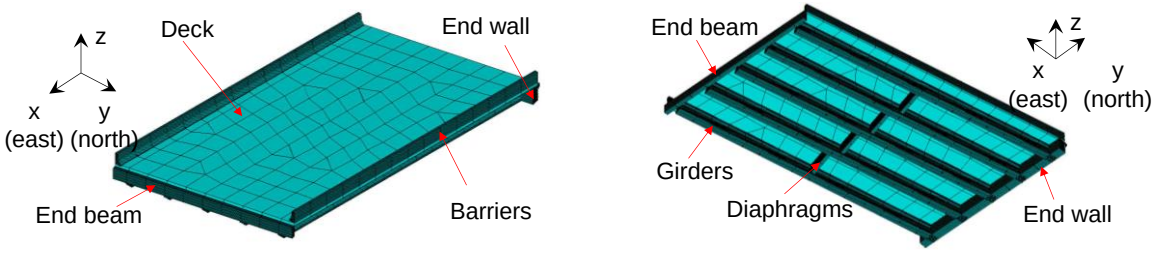

(a) (b)

FIGURE 1-8 Finite element model built in ANSYS: (a) top view; (b) bottom view

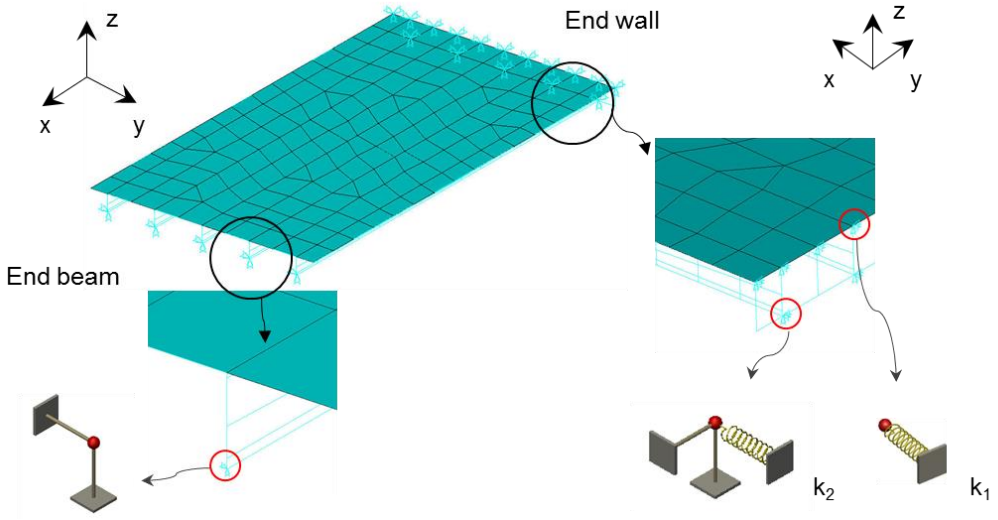

FIGURE 1-9 Illustration of boundary conditions

TABLE 1-1 Initial values of the spring stiffness constants

Spring	Stiffness (kips/in)
k_1	7.466×10^4
k_2	7.466×10^4

Each girder contains 28 pre-stressed steel strands, including 2 straight strands near the top, 6 draping strands in the middle, and 20 straight strands near the bottom (FIGURE 1-10(a)). To simplify the modeling, the top 2 strands were combined into one, the 6 draping strands were combined into one, and the 20 bottom strands were combined into one (FIGURE 1-10(b)). The cross section of the combined strands was properly configured to

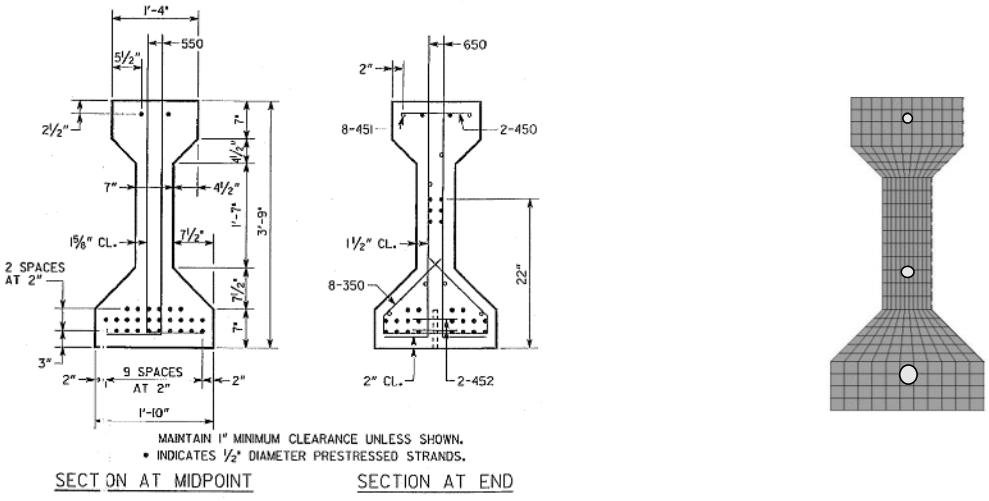

(a) (b)

FIGURE 1-10 Simplification on pre-stressed strands: (a) original drawing; (b) ANSYS simplification

reflect the overall effect. The positions of the pre-stressed strands are shown in FIGURE 1-10(b).

The bridge consists of high-strength concrete used for pre-stressed girders, and normal concrete used for other concrete components, such as the deck, barriers, diaphragms, end beam, and end wall. The pre-stressed strands are steel. The initial/nominal material properties are listed in TABLE 1-2.

Using the initial FE model, the first four vibration modes were simulated and are shown in FIGURE 1-11. The mode shapes matched well with the experiment results in FIGURE 1-7, but the resonance frequencies were relatively lower than the experiment

TABLE 1-2 Material properties

Components	Density (lbs/in^3)	Young's Modulus (ksi)	Poisson's Ratio	Coefficient of thermal expansion (1/°F)
Pre-stressed Concrete Girder (E_{c1})	0.0868	4.415×10^3	0.2	1.2×10^{-5}
Other Concrete Components (E_{c2} and E_{c3})	0.0868	3.372×10^3	0.2	1.2×10^{-5}
Pre-stressed Strand (E_s)	0.28	2.9×10^4	0.3	0.67×10^{-5}

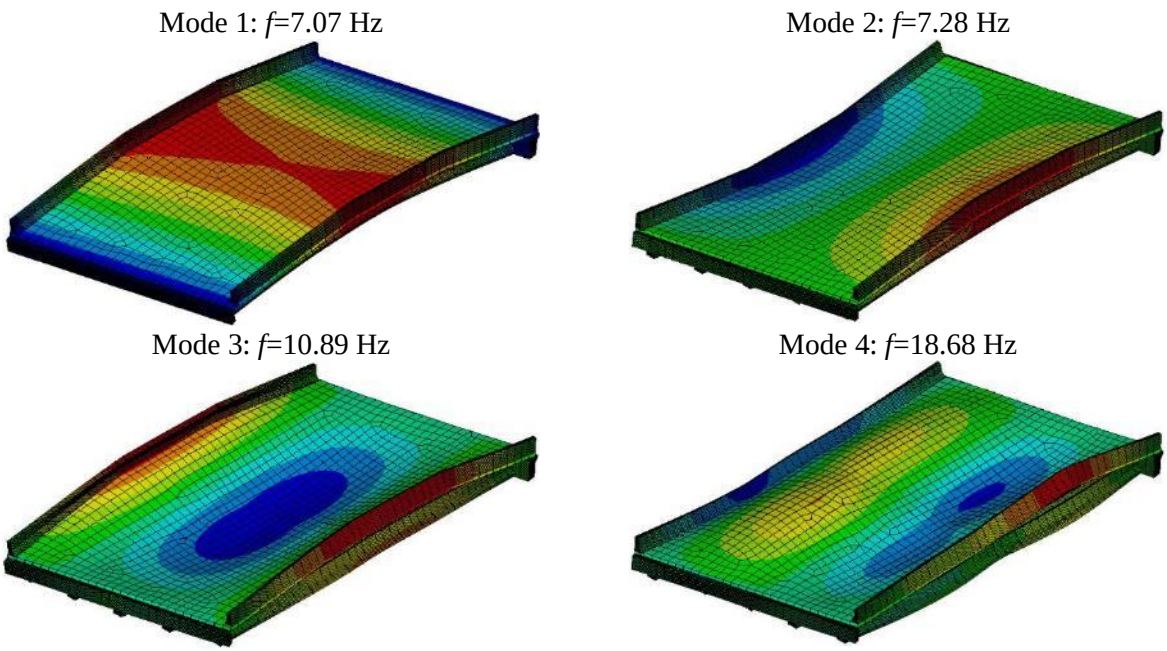

FIGURE 1-11 Simulated vibration modes

results. Therefore, FE model updating was needed to obtain more accurate material properties than the initial model with nominal parameter values.

1.4.2 Finite element model updating

The modal property difference approach was adopted for FE model updating. The approach minimizes the differences between eigenvalues and mode shapes from the experiment results and the FE simulation. Eq. 1-1 shows the objective function for the optimization problem.

$$\underset{\boldsymbol{\alpha}}{\text{minimize}} \quad \sum_{i=1}^{n_{\text{modes}}} \left\{ \left(\lambda_i^{\text{FE}} - \lambda_i\right)^2 \cdot w_i^2 + \left(\frac{1-\sqrt{\text{MAC}_i}}{\text{MAC}_i} \cdot 10^4 \right)^2 \cdot w_i^2 \right\} \qquad 1\text{-}1$$

$$\text{subject to} \quad \text{MAC}_i = \frac{\left\{(\boldsymbol{\psi}_i)^{\text{T}} \boldsymbol{\psi}_i^{\text{FE}}\right\}^2}{\|\boldsymbol{\psi}_i\|_2^2 \left\|\boldsymbol{\psi}_i^{\text{FE}}\right\|_2^2} \quad , \quad i = 1, \dots, n_{\text{modes}}$$

$$L_{\boldsymbol{\alpha}} \leq \boldsymbol{\alpha} \leq U_{\boldsymbol{\alpha}}$$

Variables λ_i^{FE} and λ_i represent the eigenvalues from the FE simulation and from the experiment results, respectively. Modal assurance criterion (MAC) was applied to evaluate how close the simulated mode shapes $\boldsymbol{\psi}_i^{\mathrm{FE}}$ match the experiment results $\boldsymbol{\psi}_i$ at measured locations (degrees-of-freedom). Four modes were included in this updating (i.e., $n_{\mathrm{modes}} = 4$). Weighing factor w_i was assigned to each mode, as $w_1 = w_2 = 5$, $w_3 = 2$, and $w_4 = 1$. The number of measured degrees-of-freedom was 15, corresponding to the 15 accelerometer locations at the bridge.

Using the optimization toolbox in MATLAB, optimal values of the bridge parameters could be obtained. TABLE 1-3 shows the comparison between the initial parameter values and the updated values of the FE model parameters. The parameters included three concrete elastic moduli (Ec1, Ec2, and Ec3), one elastic modulus of the pre-stressed steel strands (Es1), and two support spring stiffness (k1 and k2), as shown in FIGURE 1-9. Initial (nominal) parameter values from TABLE 1-1 and TABLE 1-2 are repeated here for convenience. TABLE 1-4 summarizes the natural frequencies obtained from the experiment, the initial FE model, and the updated FE model. After model updating, the simulated resonance frequencies matched better with the experiment results. Upon

TABLE 1-3 Model updating results

Updating FE model parameters		**Initial value**	**Updated value**
Elastic moduli of members along the bridge (ksi)	E_{c1} – concrete girders	4.415×10^3	5.565×10^3
	E_{c2} – concrete deck, diaphragms, end beam, end wall	3.372×10^3	3.167×10^3
	E_{c3} – concrete barrier	3.372×10^3	4.948×10^3
	E_{s1} – pre-stressed strands	2.9×10^4	3.086×10^4
Support springs (kips/in.)	k_1 – deck at end wall side	7.466×10^4	4.600×10^5
	k_2 – girder at end wall side	7.466×10^4	4.821×10^5

TABLE 1-4 Comparison of resonance frequencies and mode shapes

	f_1	f_2	f_3	f_4	MAC_1	MAC_2	MAC_3	MAC_4
Experiment	7.56Hz	8.21Hz	11.85Hz	18.99Hz	/	/	/	/
Initial FE	7.07Hz	7.28Hz	10.89Hz	18.68Hz	0.96	0.97	0.97	0.89
Error from experiment (%)	6.48%	11.33%	8.10%	1.63%	/	/	/	/
Updated FE	7.77Hz	7.99Hz	11.51Hz	19.28Hz	0.96	0.97	0.96	0.91
Error from experiment (%)	2.70%	2.58%	2.85%	1.52%	/	/	/	/

updating, the MAC values showed relatively small change, meaning the simulated mode shapes still matched well with the experimental ones.

1.5 Summary

This chapter first introduced the highway bridge where the *Martlet* wireless sensing system is instrumented. The test results show that the sensor data collected by the wireless sensing system is reliable and has the potential for detecting truck weight. In addition, modal properties of the highway bridge are obtained using the acceleration responses collected by the wireless sensing system. Finally, an accurate finite element model is achieved by minimizing the difference between experimental modal properties (from the field test) and the analytical modal properties (from the simulation model).

2 Field Testing of Bridge Weigh-in-Motion with Wireless Sensing System

This chapter presents the field validation of the bridge weigh-in-motion with wireless sensing system. The same highway bridge presented in Chapter 1 was selected for the field validation tests. Two three-axle trucks manufactured by International (7600 6×4 and 2674 6×4) were adopted as the benchmark vehicles to validate the BWIM system. In this chapter, the test vehicles are introduced first, followed by the instrumentation plan of the wireless sensing system. Finally, the results of the BWIM analysis using the data collected from the field tests are presented.

2.1 Inspection vehicle introduction

Two vehicles manufactured by Navistar International Transportation Corp. (Models 7600 6×4 and 2674 6×4) were adopted for the BWIM validation experiments (FIGURE 2-1(a)). FIGURE 2-1(b) shows the key dimensions of the two vehicles (i.e., distance between axles). Prior to the validation tests, the weight of each vehicle was measured by portable scales (TABLE 2-1).

2.2 Stationary wireless sensing system on the bridge

As shown in FIGURE 2-2(a), the highway bridge was instrumented with strain gages to measure the structural responses of the bridge introduced by the inspection vehicle. A total of 19 strain gages were instrumented under the bottom of the girders (FIGURE 2-2(a) and (b)). Furthermore, the corresponding *Martlet* wireless nodes were protected by

Half-loaded truck (2600 6×4)

Fully loaded truck (7600 6×4)

(a)

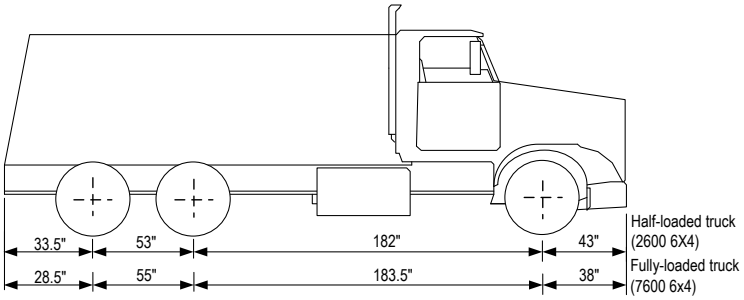

(b)

FIGURE 2-1 Inspection vehicles: (a) photos of the trucks; (b) key dimensions of the trucks

TABLE 2-1 Vehicle axle weights

Vehicle number	Axle weight (lb)			
	Total weight	1st axle	2nd axle	3rd axle
Half-loaded truck (2674 6×4)	36,400	15,100	10,800	10,500
Fully loaded truck (7600 6×4)	45,200	16,150	14,950	14,100

weatherproof boxes and attached to the girders. FIGURE 2-2(c) and (d) show the close-up views of the strain gages installed at several locations.

In addition, truck position sensors were installed on top of the bridge to accurately locate the truck position during the tests. A set of truck position sensors was composed of

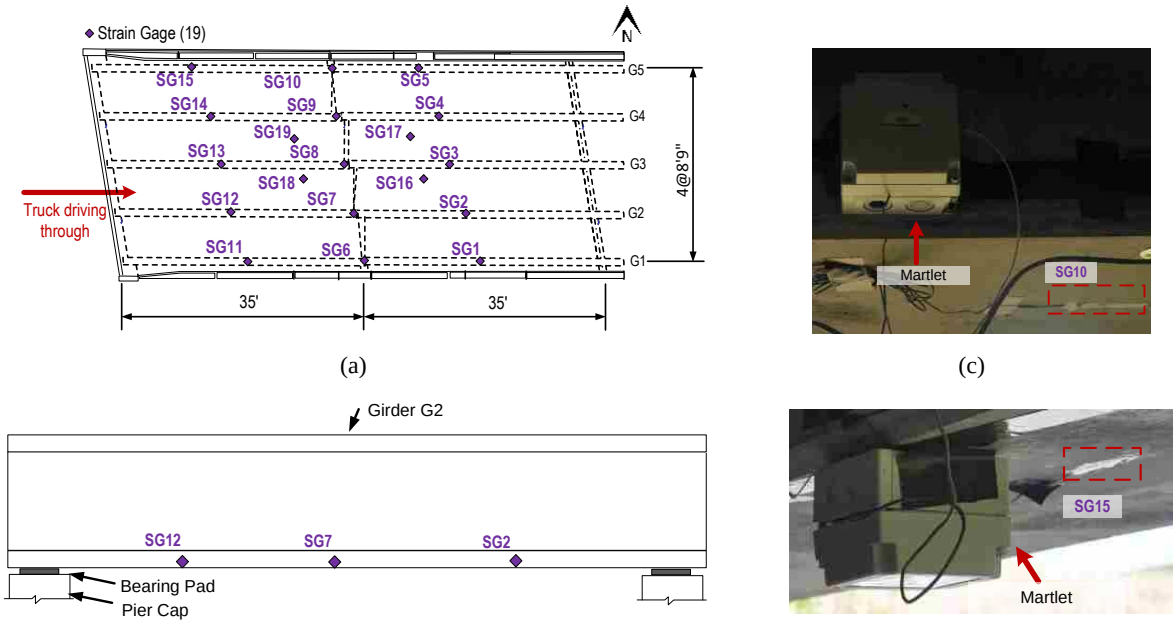

FIGURE 2-2 Summary of instrumentation: (a) instrumentation plan; (b) elevation view of girder G2; (c) strain gage SG10; (d) strain gage SG15

two parts, sitting at opposite sides of the road: a laser emitter and a laser receiver (FIGURE 2-3(a) and (b)). When the vehicle drove through the position sensor, the laser signal from the emitter would be blocked by the vehicle. Accordingly, there would be a drop in the receiving signal from the laser receiver. As a result, the position of the truck on the bridge during the test could be determined. In total, there were 5 truck position sensors installed on top of the bridge (FIGURE 2-3(c) and (d)).

(a) (b)

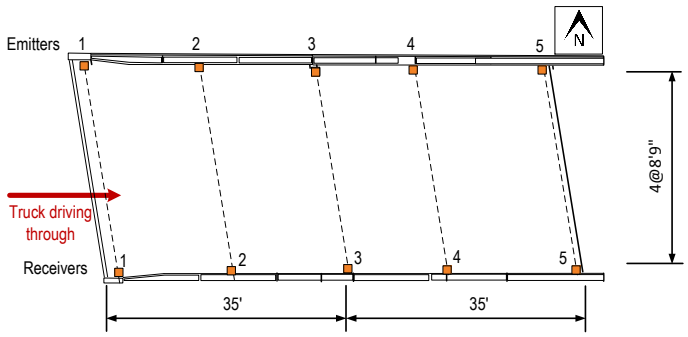

(c)

(d)

FIGURE 2-3 Truck position sensor: (a) laser emitter; (b) laser receiver; (c) instrumentation plan; (d) laser receiver installed on the bridge

2.3 BWIM analysis

2.3.1 Bridge modeling

For bridge weight-in-motion analysis, a 3-D solid element was used to simulate the bridge using the LS-DYNA finite element program. To verify the model accuracy, two 3-axle trucks (one fully loaded and one half-loaded) were used (FIGURE 2-4).

FIGURE 2-4 Half- and fully loaded vehicles

The two vehicles drove along lane 1, which is above girder G3 and close to G2 (see FIGURE 1-2(a)). The sampling frequency of the data acquisition system was 200 Hz. To compare the simulated strain with the measurement, in this simulation the half and fully

loaded trucks passed over the bridge at 35.0 mph. The researchers simulated the truck by 6 moving loads representing the wheel load using the actual axle distances and the actual wheel loads (FIGURE 2-5)

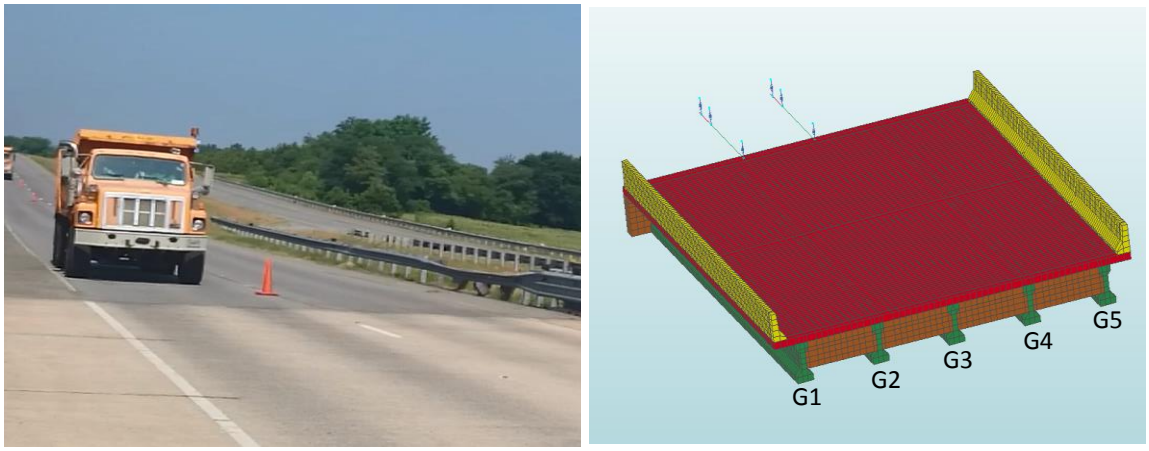

FIGURE 2-5 Actual and simulated vehicle bridge interaction

The research team plotted the strain collected from the field and the strain simulated by model, as shown in FIGURE 2-6 to FIGURE 2-9. The simulated strain data and the corresponding measurement matched well in both waveform and magnitude, at all five girders and for both trucks.

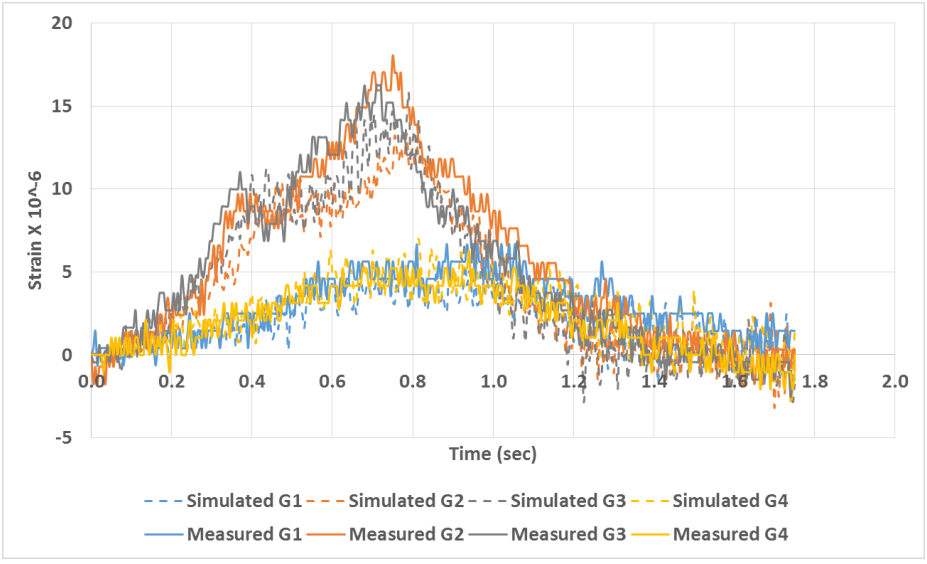

FIGURE 2-6 Strain comparison at L/4 of the bridge span due to half-loaded truck

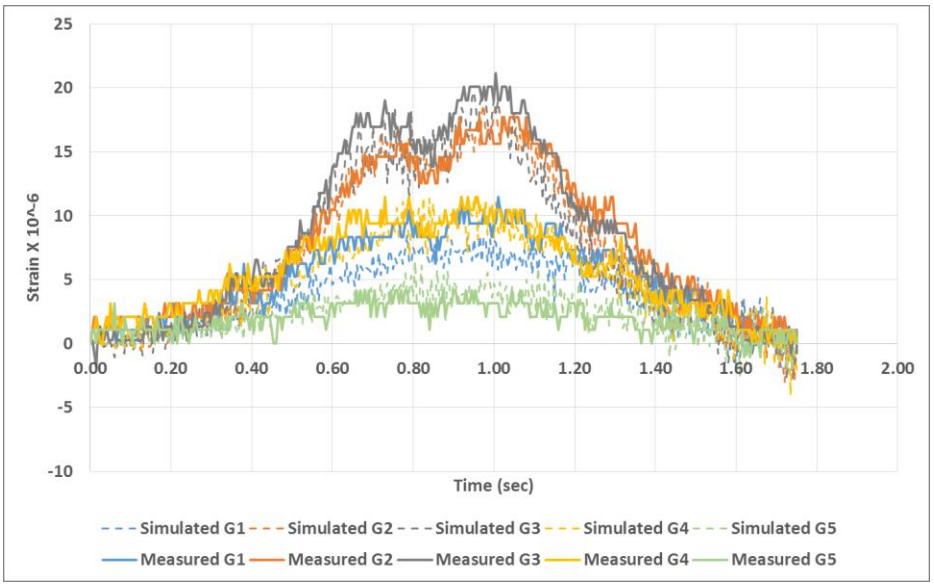

FIGURE 2-7 Strain comparison at L/2 of the bridge span due to half-loaded truck

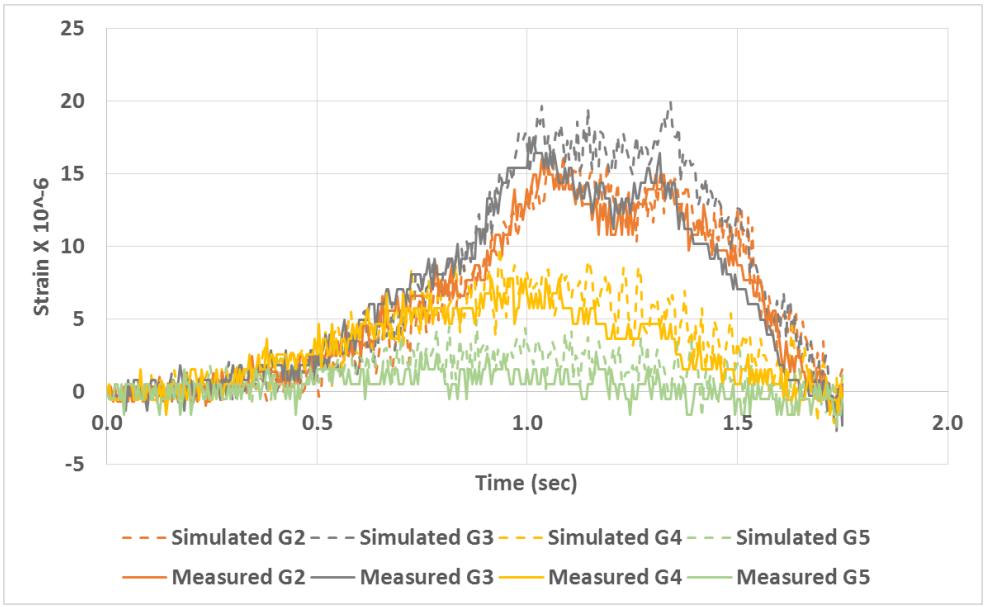

FIGURE 2-8 Strain comparison at 3L/4 of the bridge span due to half-loaded truck

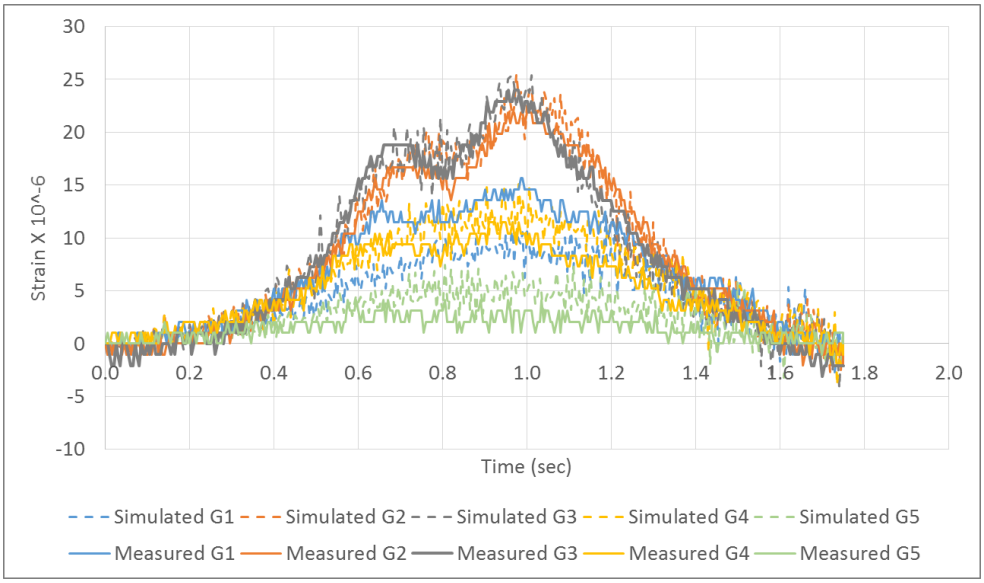

FIGURE 2-9 Strain comparison at L/2 of the bridge span due to fully loaded truck

2.3.2 Moving force identification for BWIM analysis

After the researchers verified the accuracy of the bridge FEM model, they selected a finite number of modes to reduce the order of the bridge dynamic system. The modes were used in the moving force identification (MFI) algorithm associated with dynamic programming and the Tikhonov regularization method. Rowley demonstrated that the first 25 modes can usually provide sufficient accuracy in moving force identification with the application of first-order regularization technique [5]. In the following investigation, the research team considered 25 modes to reduce the order of the dynamic system. In essence, the MFI algorithm searches for axle load values that cause the FEM model to generate the same strain as measured by the sensors on the bridge girders.

2.3.3 Field testing of MFI with half-loaded truck

The researchers first applied the measured mid-span strain data at the girders to test the accuracy of the MFI algorithm in calculating the truck axle loads. The strain data for

the five girders were plotted, as shown in FIGURE 2-10. The data were collected when the half-loaded truck drove across the bridge at 35 mph.

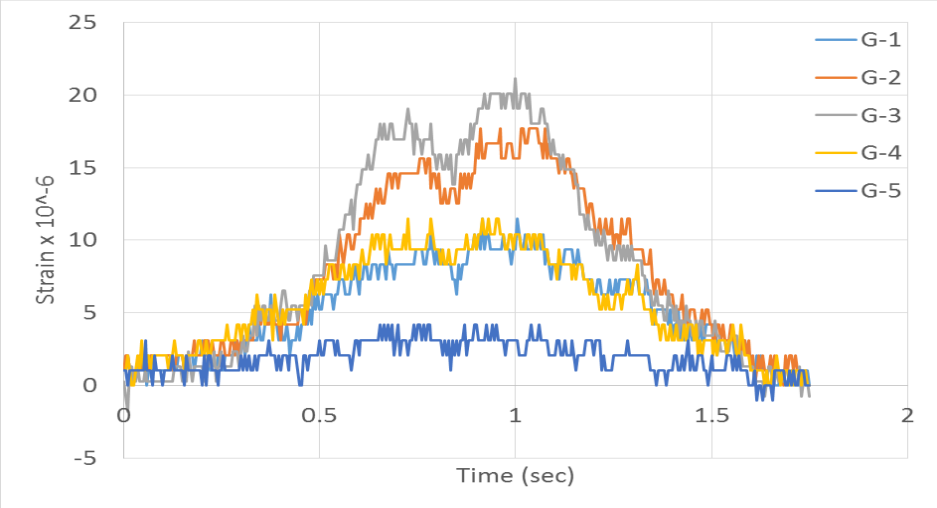

FIGURE 2-10 Strain measurements at L/2 span for the half-loaded truck

The calculated axle loads were plotted as shown in FIGURE 2-11. Because the axles have close spacing (axles 2 and 3), the researchers summed these two wheel loads together.

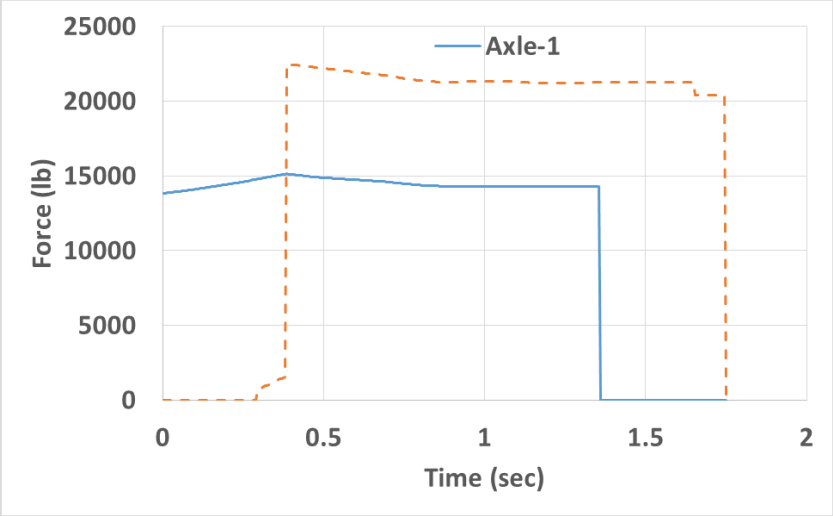

FIGURE 2-11 Force history of the half-loaded truck

TABLE 2-2 shows the comparison between the static load and the calculated force history for the axles and the total truck weight. The results were very good as the identification errors in the truck gross vehicle weight (GVW) and the axle loads were all small. The axle loads were calculated using the average of the middle 60% of the force history.

TABLE 2-2 Comparison between the static and calculated loads of half-loaded truck

Item	Static weight (lb)	Calculated weight (lb)	Error (%)
Axle-1	15,100	14,623	−3.15
Axles 2+3	21,300	21,358	+0.27
Gross vehicle weight (GVW)	36,400	35,981	−1.14

2.3.4 Field testing of MFI with fully loaded truck

This subsection studies the scenario when the fully loaded truck passed across the bridge at 40 mph. The measured mid-span strain data at the girders were collected and plotted as shown in FIGURE 2-12.

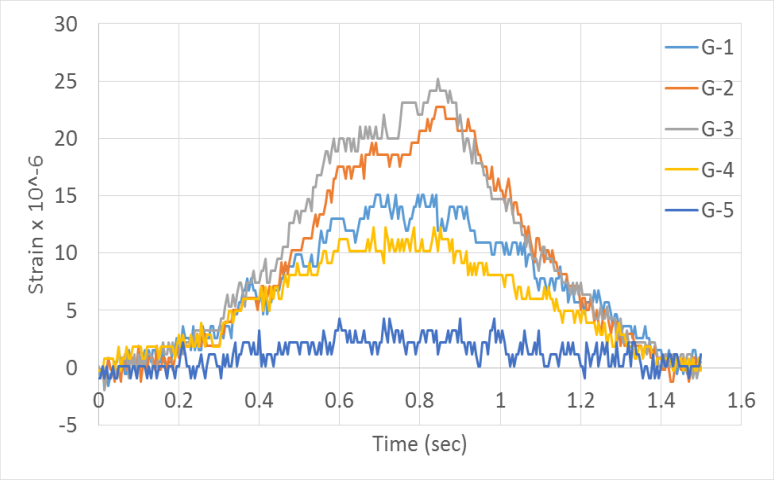

FIGURE 2-12 Strain measurements at L/2 span for the fully loaded truck

The calculated axle loads were plotted as in FIGURE 2-13, and TABLE 2-3 shows the comparison between the static load and the calculated force history for the axles and the total truck weight. Also, the table shows good results for both the axles and the total weight.

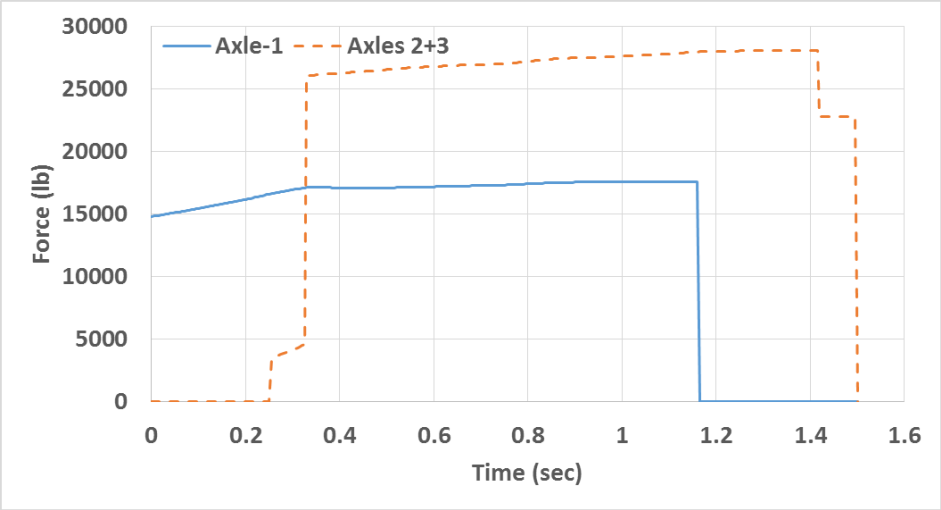

FIGURE 2-13 Force history of the fully loaded truck

TABLE 2-3 Comparison between the static and calculated loads of the fully loaded truck

Item	Static weight (lb)	Calculated weight (lb)	Error (%)
Axle-1	16,150	17,162	−6.26
Axles 2+3	29,050	27,336	+5.89
GVW	45,200	44,498	+1.55

2.3.5 Effect of a small vehicle on the truck weight calculation

Sometimes when the test truck crossed the bridge, there was public traffic passing through at the same time. To calculate the effect of an extra vehicle on the BWIM accuracy, the researchers considered the case when the half-loaded truck at 38 mph was accompanied by a small vehicle, as shown in FIGURE 2-14. Neither the speed nor the weight of the

small vehicle was known. The strain measurements collected at the L/2 location of the bridge girders were plotted as in FIGURE 2-15.

FIGURE 2-14 Small vehicle passing beside the truck

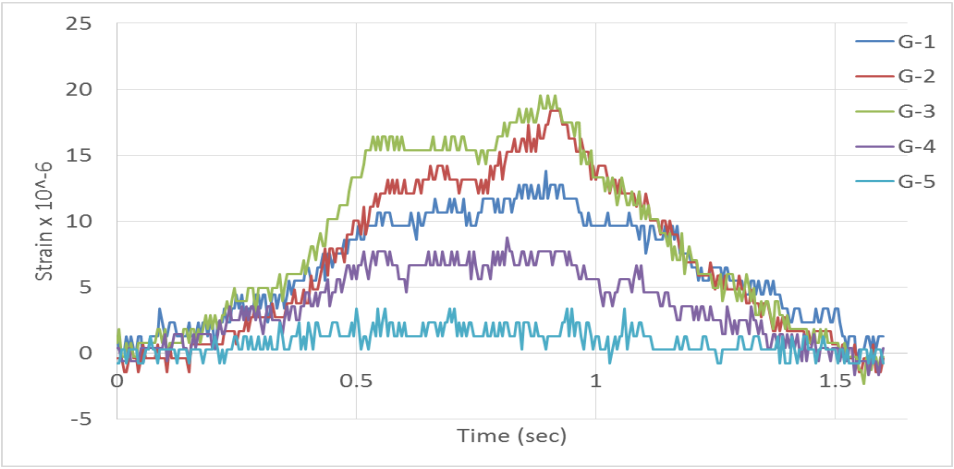

FIGURE 2-15 Strain measurements at L/2 span for the half-loaded truck

The calculated axle loads were plotted as in FIGURE 2-16. TABLE 2-4 shows the comparison between the static load and the calculated force history for the axles and the total truck weight.

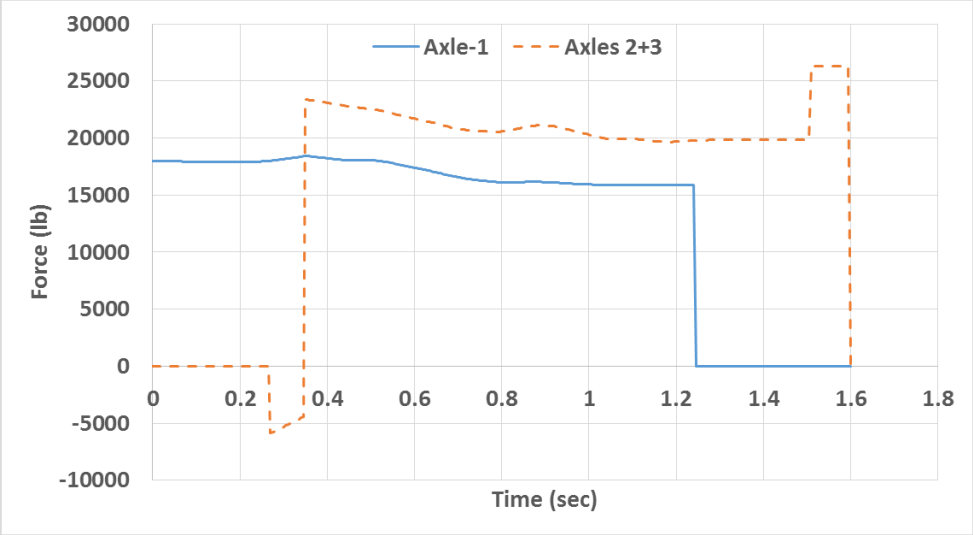

FIGURE 2-16 Force history of the half-loaded truck

TABLE 2-4 Comparison between the static and calculated loads

Item	Static weight (lb)	Calculated weight (lb)	Error (%)
Axle-1	15,100	17,005	12.61
Axles 2+3	21,300	20,323	−4.5
GVW	36,400	37,328	2.55

From the table, the effect of the small vehicles on the truck weigh calculation was no more than 13% in axle weight, and more importantly, less than 5% in the truck total weight.

2.3.6 Effect of two trucks crossing the bridge at the same time

A more challenging scenario was when a heavier vehicle was passing by and affected the BWIM accuracy. In this subsection, the research team considers when two heavy trucks crossed over the bridge at the same time (see FIGURE 2-17).

FIGURE 2-17 Two trucks crossing the bridge at the same time

The test shown in FIGURE 2-17 represents the case as the two trucks (half- and fully loaded) passed the bridge side by side at two different speeds (30.64 mph and 24.6 mph, respectively). The fully loaded truck entered the bridge first in lane 2, followed by the half-loaded truck in lane 1. The strain measurements collected from the field at the L/4, L/2, and 3L/4 locations of the five girders were plotted as in FIGURE 2-18 through FIGURE 2-20.

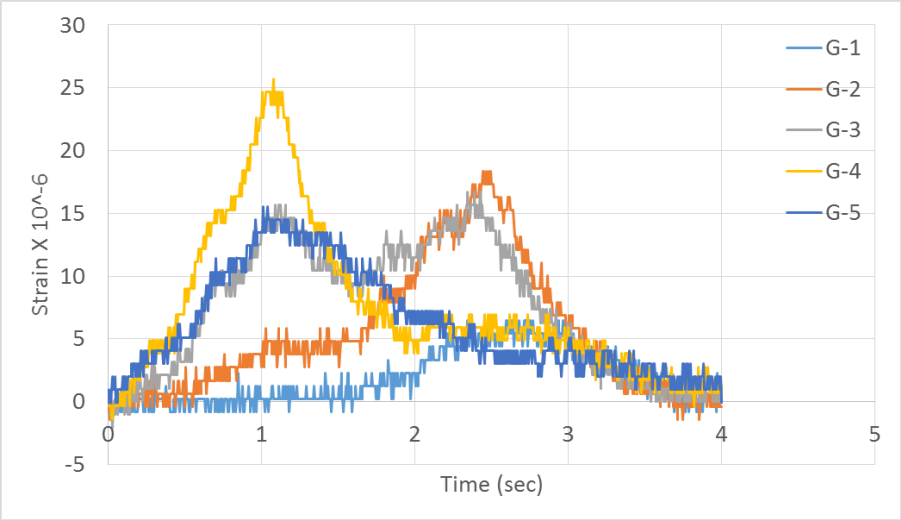

FIGURE 2-18 Strain measurements at L/4

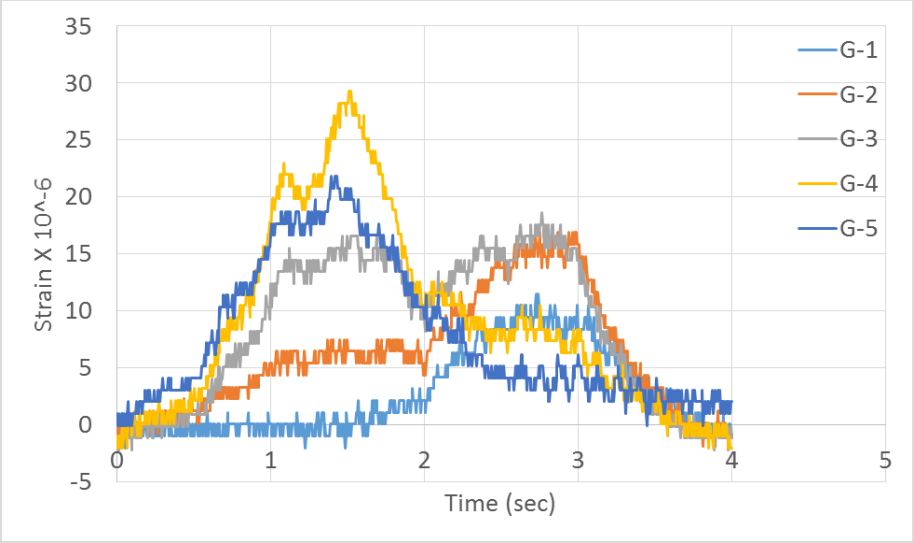

FIGURE 2-19 Strain measurements at L/2

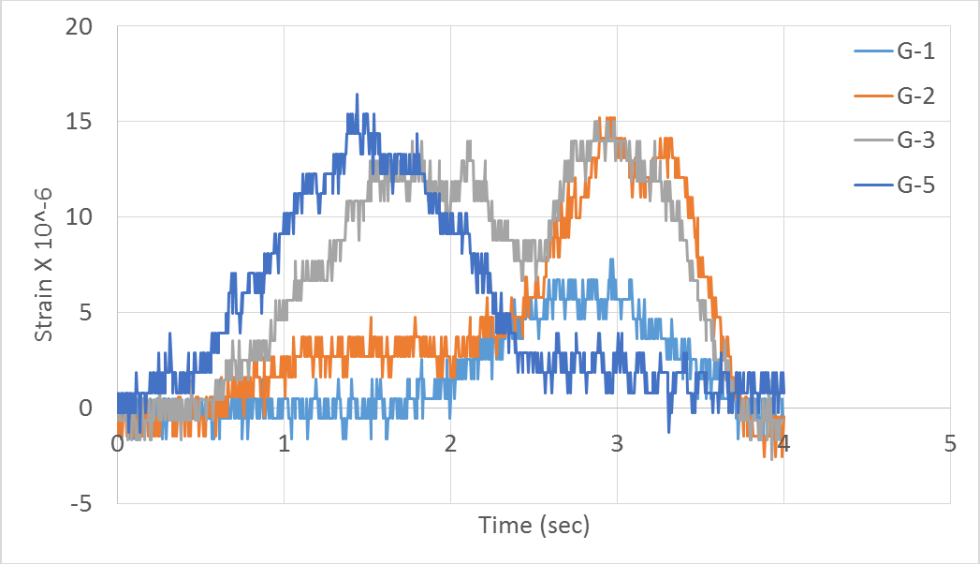

FIGURE 2-20 Strain measurements at 3L/4

The calculated axle loads were plotted as in FIGURE 2-21 and FIGURE 2-22, and TABLE 2-5 shows the comparison between the static load and the calculated force history for the axles and the total truck weight.

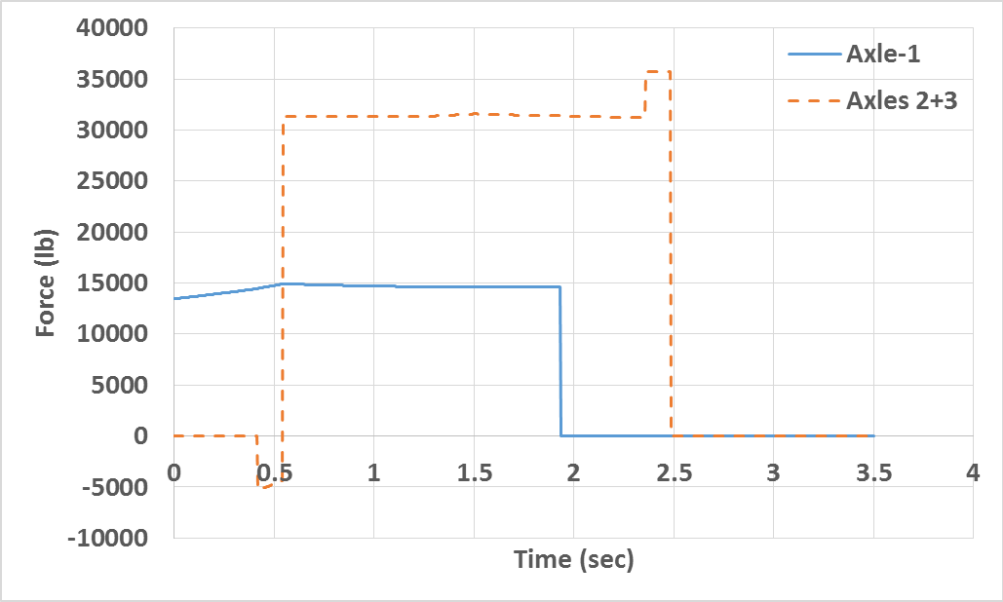

FIGURE 2-21 Force history of the first truck – fully loaded

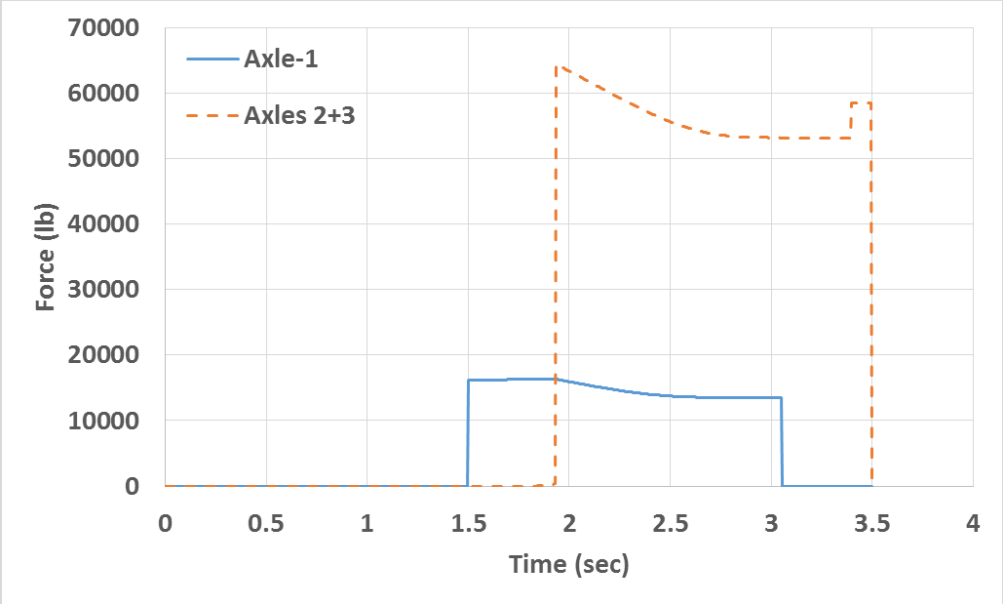

FIGURE 2-22 Force history of the second truck – half-loaded

TABLE 2-5 Comparison between the static and the calculated loads

Item	Fully loaded			Half-loaded		
	Static weight (lb)	Calculated weight (lb)	Error (%)	Static weight (lb)	Calculated weight (lb)	Error (%)
Axle-1	16,150	14,689	−9.04	15,100	14,710	−2.58
Axles 2+3	29,050	31,420	8.16	21,300	55,144	158
GVW	45,200	46,110	2.01	36,400	69,854	91.9

From the table, it is evident that the MFI algorithm identified the fully loaded truck (which entered the bridge first) with high accuracy in both the axles and in gross vehicle weight; on the other hand, the algorithm gave a poorer identification for the second truck. This may be because when the second truck enters the bridge, the bridge was already excited by the first truck. In order to improve the estimation results, the dynamic influence line (IL) is used to separate strain signals from the two trucks. The weight of the first truck from a previous MFI run is used to estimate the strain response caused by the first truck, which is then subtracted from the original signal to get the strain response caused by the second truck. The MFI algorithm is then used again to estimate the second truck weight. The dynamics IL method was first introduced by O'Brien et al. in 2006 [6], who proposed a mathematical method to derive the IL from experiment measurements. These measurements must be caused by a vehicle of known weight and axle spaces. Based on the measruements, the error between the theoretical load effects (strains) and measured ones is calculated. Least square method is then used to minimize the summation of the square of the error. The ordinates of IL are found by solving a large set of simultaneous equations [7]. FIGURE 2-23 shows the strain measurements at mid-span due to the fully loaded truck in the second lane, which is used to calculate the ILs for the girders. FIGURE 2-24 shows

the theoretical and the calculated ILs. FIGURE 2-25 illustrates the predicted strain response from the five girders caused by the first truck (fully loaded) by using the calculated dynamic ILs.

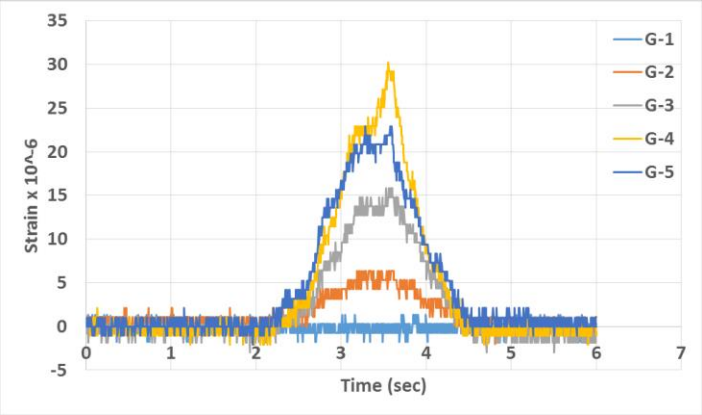

FIGURE 2-23. Strain measurements at mid-span due to the fully loaded truck in the second lane.

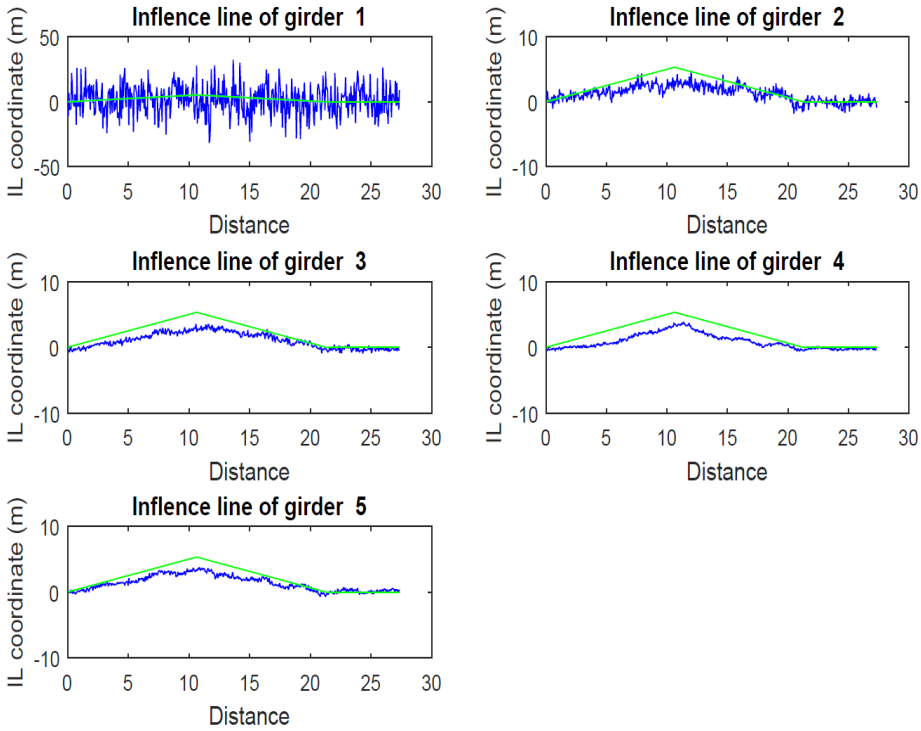

FIGURE 2-24 Theoretical and calculated ILs (truck in lane 2)

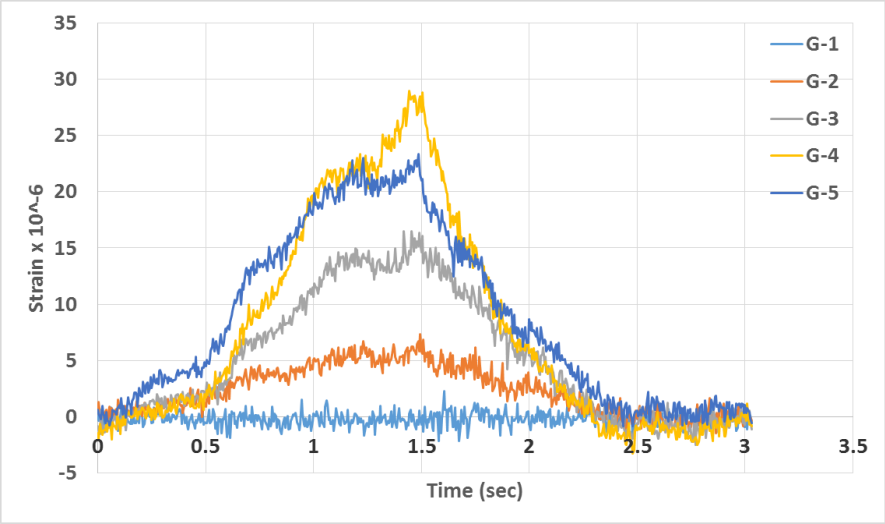

FIGURE 2-25 Predicted strain response of the five girders at mid-span (fully loaded truck)

FIGURE 2-26 shows the estimated strain responses from the five girders due to the second truck (half-loaded) alone, which was calculated by subtracting the estimated strain caused by the fully loaded truck from the original strain measurements.

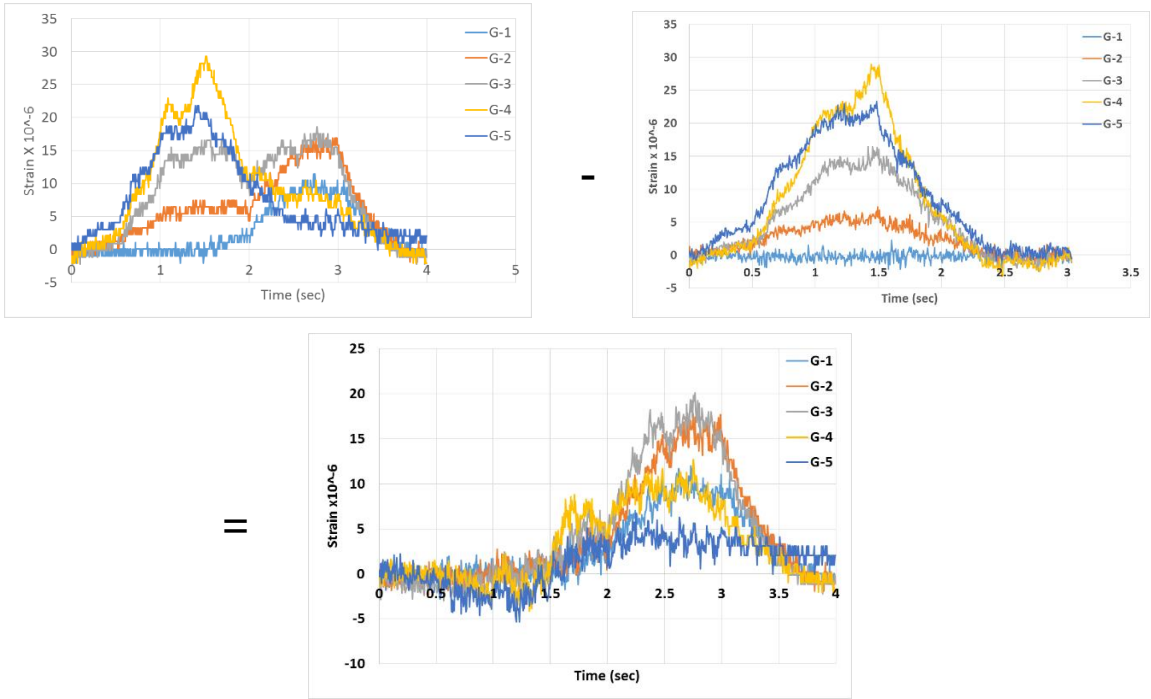

FIGURE 2-26 Strain response due to the second truck (half-loaded) alone

The subtracted strain response is then used to calculate the second truck weight except the strain response of girder G4. The results are plotted in FIGURE 2-27. TABLE 2-6 shows the comparison between the static load and the calculated force history for the axles and the gross vehicle weight. Also, the table indicates that the results are good in terms of both the axles and gross vehicle weight.

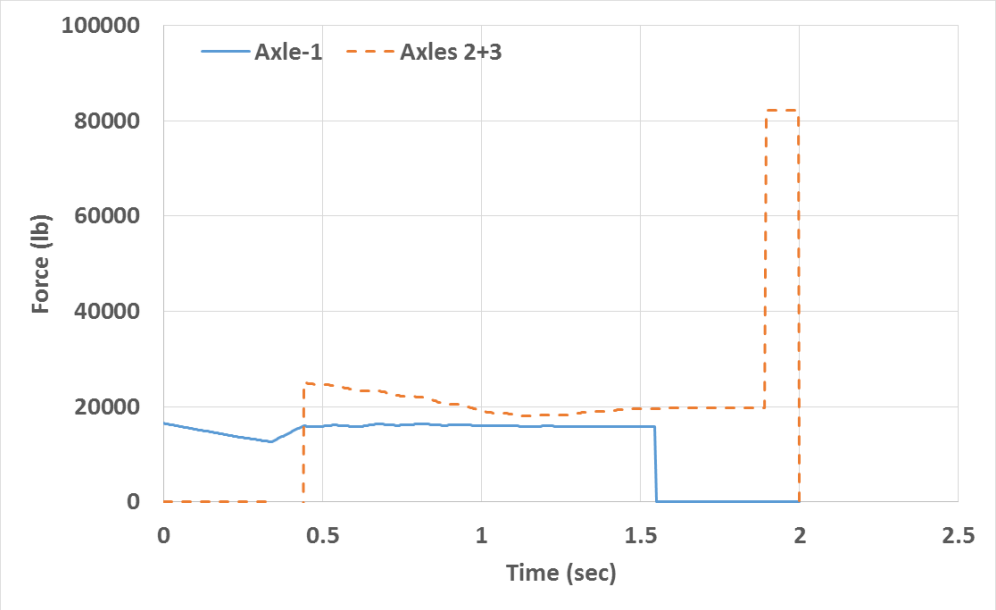

FIGURE 2-27. Force history of the second truck – half-loaded truck.

TABLE 2-6 Comparison between the static and calculated loads

Item	Static weight (lb.)	Calculated weight (lb.)	Error (%)
Axle-1	15,100	15,866	5.07
Axles 2+3	21,300	19,278	-9.49
GVW	36,400	35,145	-3.44

To enhance the IL calculation and to get more accurate ILs for girders, statistical studies are needed in the future using a large number of measurements. This is because the ILs of the girders utilize the transverse positions of the trucks to calculate the distributions factors, which are used to distribute the axle's loads to the girders. In this case, a large number of runs are needed to cover all possible cases.

2.4 Summary

In conclusion, the moving force identification algorithm detected the axles and total weight with high accuracy in most cases. This chapter discussed the effect of a small vehicle that passed the test truck on the bridge, which was an effect of less than 10% on the truck weight estimation. Finally, this chapter discussed the case when two heavy trucks passed over the bridge at the same time with different speeds. The algorithm detected the first truck more accurately than the second truck.

In order to improve the estimation results in the case when two heavy trucks passed over the bridge, dynamic influence lines are used to separate strain effects caused by the two trucks and the MFI algorithm is then used to detect the weight of the second truck. The estimation results were significantly improved with the error dropping to less than 10% for both axle weights and gross vehicle weights for the second truck.

3 Vehicle Drive-by Inspection

3.1 Introduction

Bridges are subject to continuous degradation due to the unremitting increase in the traffic volume, and the effects of environmental and hazardous events. In the United States, there are about 66,405 structurally defective bridges; this number is more than 11% of the total number of bridges in the US transportation network [8]. This current status raises the importance of monitoring the structural health condition for bridges using Structural Health Monitoring (SHM) techniques [9]. Traditional SHM techniques are based on sensor instrumentation on the bridge structure, which limits the number of inspected bridges.

Recently, there is a trend to shift the instrumentation from the bridge to a passing vehicle to monitor the bridge structural condition. This technique is known as "drive-by bridge inspection" [10]. One of the first studies in this field was performed by Yang et al. [11, 12], who investigated the feasibility of extracting the bridge fundamental frequencies from the acceleration history of a crossing vehicle. They validated the approach theoretically using a closed solution of the vehicle–bridge interaction (VBI) problem, and using finite element modeling. Lin and Yang [13] asserted the observations of the theoretical study through a field test. They found that the approach works for driving speeds less than 40 km/h. Kim and Kawatani [10] used the same principle to distinguish the changes in the bridge dynamic properties due to structural damages by monitoring the change in the fundamental bridge frequency.

Since that study, many authors have investigated enhancing the approach by monitoring parameters that are more sensitive to structural damages [14-19]. However, all

the proposed approaches focus on processing the acceleration signal to extract an index related to the dynamic bridge properties. Recently, OBrien and Keenahan [20] introduced a novel concept of using a traffic speed deflectometer (TSD) to identify bridge damage. The TSD is a specialist vehicle, designed for high-speed pavement stiffness measurement, which calculates the relative distances between the road surface and a horizontal beam on the truck. Obrien and Keenahan used the TSD data to back derive the "apparent profile" (AP), defined here as the sum of the road profile and the bridge displacement time history, as measured from the moving vehicle. The approach is considered a break-through in the drive-by bridge inspection, since it calculates the changes in the bridge response due to structural damages.

Herein, the research team introduces a new method for back-calculating the AP using a number of accelerometers on a non-specialist vehicle. The approach utilized the measured vehicle accelerations to calculate the road reaction history on the vehicle axles. The road reaction history was then applied to an equivalent calibrated theoretical vehicle model. Using the Newmark-beta method of integration, the corresponding vehicle axle displacement (i.e., the AP) could be calculated. The APs found from the solution were then compared to a baseline profile obtained when the bridge was in a healthy state. The difference between the current AP and the baseline profile, referred to as the bridge displacement profile difference (BDPD), was shown to be sensitive to bridge damage and can be used as a damage indicator (FIGURE 3-1). This approach was validated using field test data from a truck crossing a highway bridge. In this chapter, first, the field test instrumentation and test scenarios are described. Next, a calibrated theoretical half-car

model was built to represent the actual truck. Finally, the measured truck accelerations were applied to the theoretical truck model to calculate the APs and BDPD.

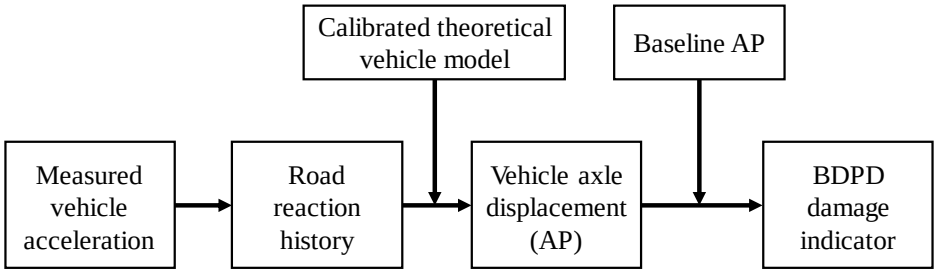

FIGURE 3-1 BDPD drive-by inspection

3.2 Field validation of the BDPD approach

In this section, the field test data are used to investigate the feasibility of using a drive-by inspection vehicle to identify the changes in the bridge dynamic properties. Since the bridge was recently constructed (2006) and has not been subjected to any hazardous events, the structural integrity is still intact. Therefore, the BDPD approach, alternatively, was investigated in identifying the changes in the bridge deformation due to different traffic configurations. Three levels of loading scenarios were investigated, as described in this section: (1) bridge deformation due to the inspection vehicle only, (2) bridge deformation due to the inspection vehicle and a small passenger vehicle, and (3) bridge deformation due to the inspection vehicle and a fully loaded truck.

3.2.1 Mobile wireless sensing system on the inspection vehicle

The inspection vehicle introduced in Section 2.1 was used to dynamically load the highway bridge. Five sensors (4 accelerometers and 1 gyroscope) were instrumented on the inspection vehicle to measure the dynamic behavior of the vehicle (FIGURE 3-2). As shown in FIGURE 3-3, the vertical acceleration of each axle was recorded by one Silicon Designs accelerometer (2012-002). In addition, to measure the vertical and horizontal

acceleration of the truck body, one integrated accelerometer was installed approximately at the center of gravity of the truck body. At the same location, another gyroscope (ADXRS624) was instrumented to capture the pitching motion of the truck (FIGURE 3-3 (b)). All the sensors on the vehicle were interfaced with a *Martlet* wireless unit to record the sensor outputs.

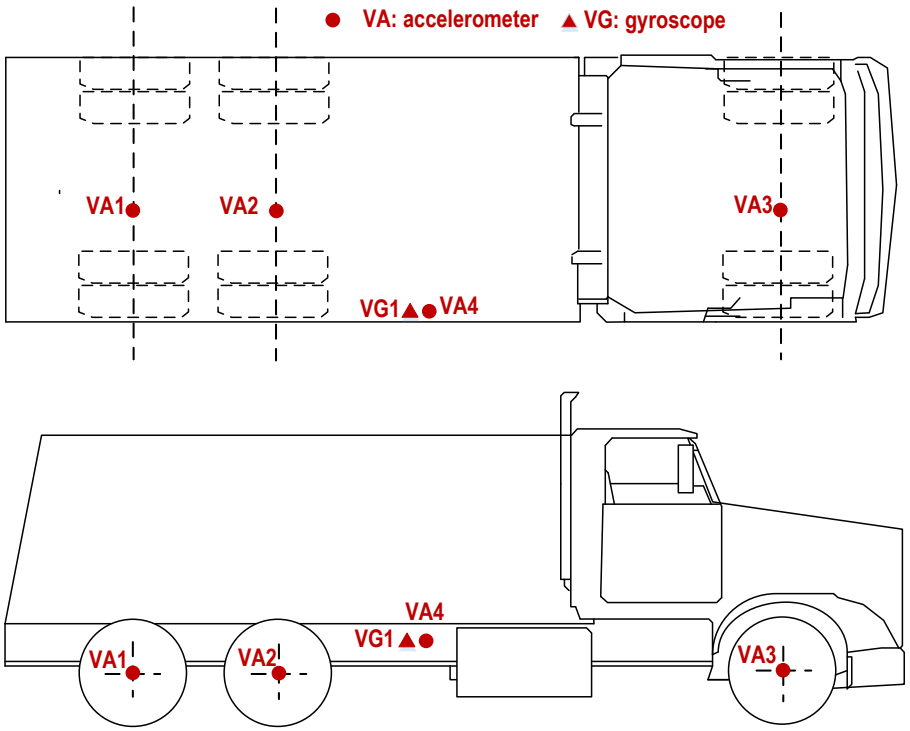

FIGURE 3-2 Mobile wireless sensor instrumentation plan

(a) (b)

FIGURE 3-3 Installation of wireless sensors on the inspection vehicle: (a) accelerometer installed on the front axle; (b) accelerometer and gyroscope installed on the truck body

3.2.2 Inspection vehicle calibration

The first step was to build a calibrated theoretical model of the inspection truck to be used in extracting the BDPDs for each loading scenario. From Section 2.1, the weight of each axle and the axle spacings are shown in FIGURE 3-4. Using these data, the center of gravity, body mass, and body inertia of the truck were calculated as shown in TABLE 3-1.

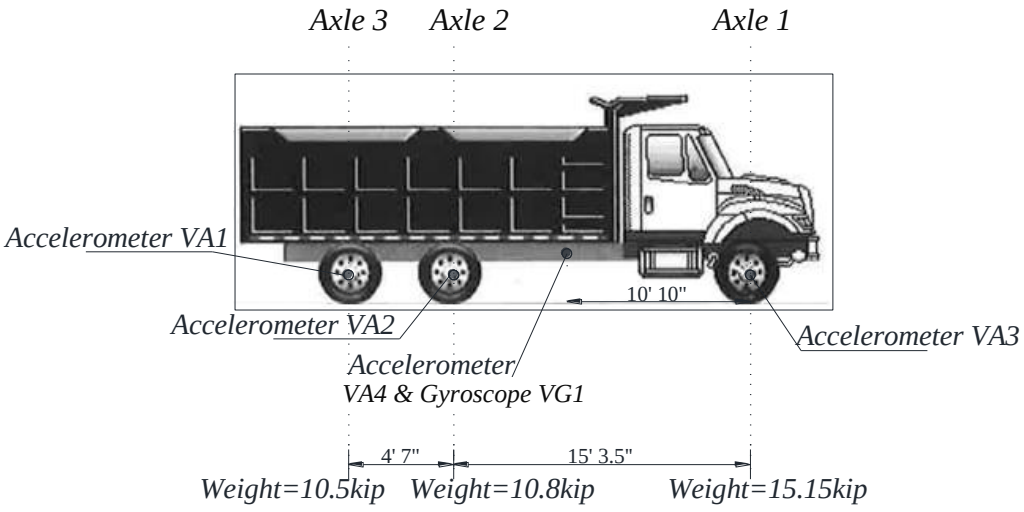

FIGURE 3-4 Axle weights

TABLE 3-1 Vehicle properties

Axle 1 mass slug **(*kg*)**	**Axle 2 mass** slug **(*kg*)**	**Axle 3 mass** slug **(*kg*)**	**Truck body mass** slug **(*kg*)**	**Truck moment of inertia** slug·ft^2 **(*kg*·*m*^{2})**	**Center of gravity from front axle** ft **(*m*)**
48.02 (700.8)	34.23 (499.6)	33.28 (485.7)	115.53 (1686.1)	8659 (11740)	10.26 (3.126)

The equivalent vehicle model needed to satisfy the same geometric and dynamic properties as the real truck. The properties in TABLE 3-1 were used for the geometrical calibration, while for calibrating the dynamic properties, the theoretical vehicle model required the same fundamental frequencies as the actual truck. The truck would be modeled using a two degrees-of-freedom (DOFs) half-car model as illustrated in FIGURE 3-5, where m_s is the truck body mass and I_s is the truck moment of inertia. Therefore, the truck bouncing and pitching frequencies were required for the calibration process.

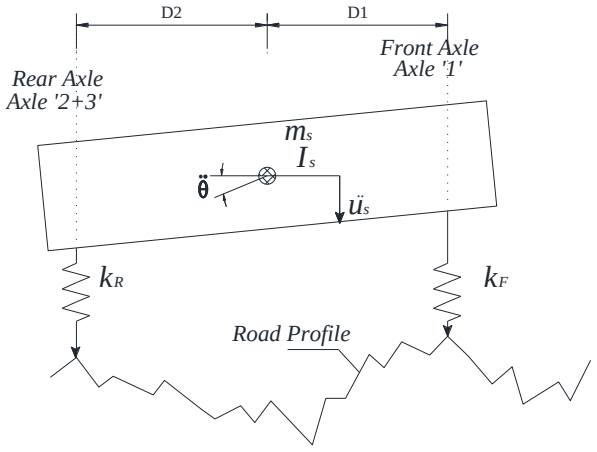

FIGURE 3-5 Half-car model

The fundamental truck frequencies could be identified from the axles and body acceleration spectra. The accelerometers measured the vertical accelerations of the front axle, the two rear axles, and the vehicle body mass. A gyroscope was also installed to

measure the pitching velocity of the truck body mass. The accelerometer locations on the truck are shown in FIGURE 3-4. The acceleration spectra would be plotted using the time history data recorded when the truck started to move until it reached the bridge span. This was to ensure that the spectra included only the truck frequencies, and would not be contaminated by the bridge frequencies.

First, for the rear axles, the signals were transferred from the time domain to the frequency domain using fast Fourier transform (FFT). The power spectra density (PSD) did not show a clear peak indicating the vehicle excitation, as shown in FIGURE 3-6. This is because the rear suspension is heavily loaded and has a high stiffness value [21], requiring a high level of vibration to be excited. Thus, there were no clear peaks in Axle 2's acceleration spectra, except one in the beginning that refers to the signal time period. However, as highlighted in FIGURE 3-6(a) and (b), a jump in the acceleration plots of Axles 2 and 3 clearly showed when the truck entered the bridge span. This information was very important to determine the data window that would be chosen for extracting the vehicle frequencies (in the period before the vehicle enters the bridge).

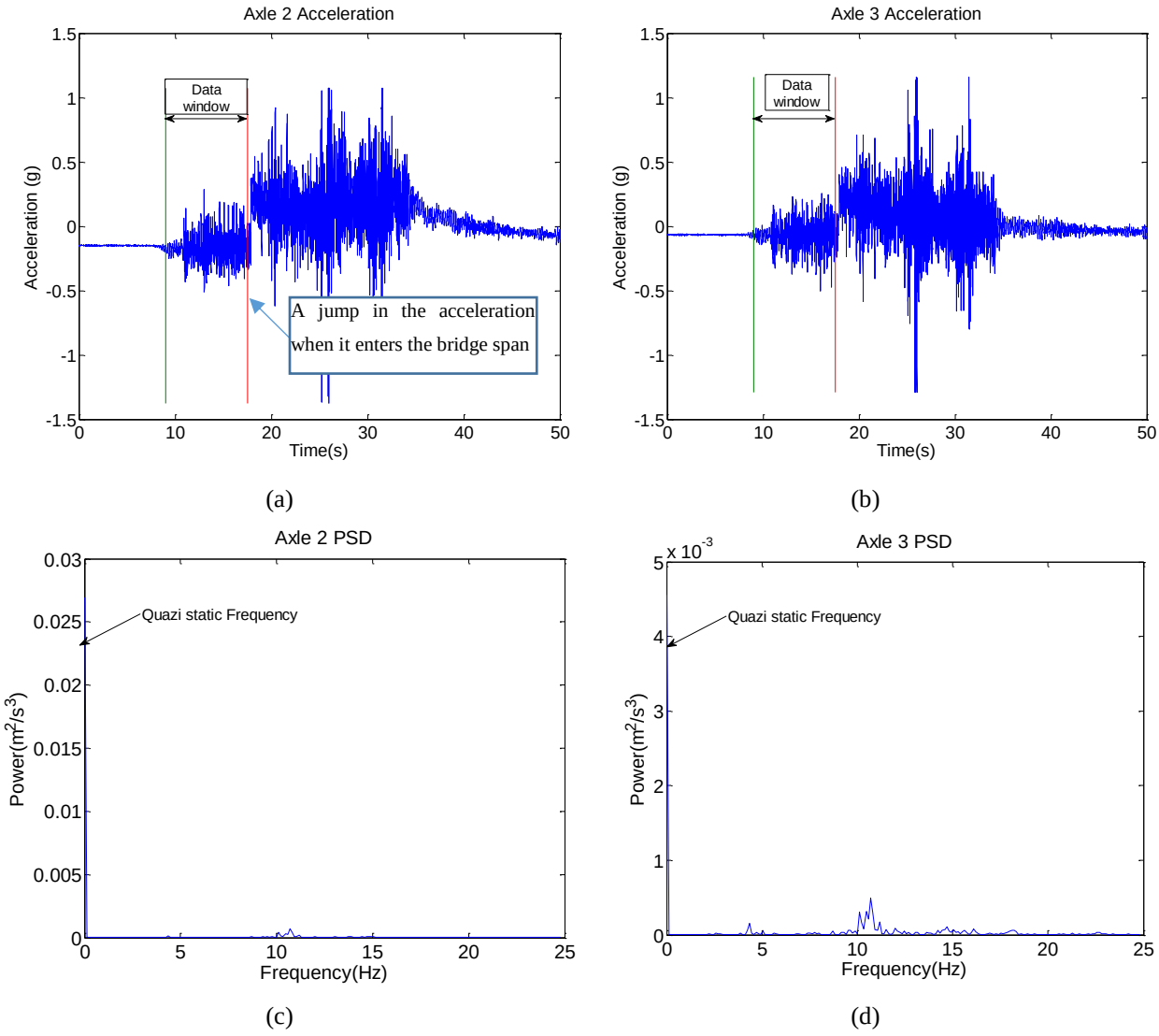

FIGURE 3-6 Rear axles acceleration: (a) axle 2 acceleration; (b) axle 3 acceleration; (c) PSD of axle 2 acceleration; (d) PSD of axle 3 acceleration

In contrast, the acceleration spectrum of Axle 1 showed peaks with considerable values (FIGURE 3-7). The dominating mode of vibration for Axle 1 was the bouncing frequency, while the pitching frequency was not clearly distinguished from this graph. The bouncing frequency was found to be 2.587 Hz, while the pitching was either 3.75 Hz or 4.35 Hz.

The process was applied to the body mass acceleration recorded by accelerometer VA4. It is noteworthy that the accelerometer was installed with a slight distance from the body mass center, which makes the measurement dominated by both body bouncing and body pitching frequencies (refer to FIGURE 3-4 and TABLE 3-1). The PSD of accelerometer VA4 is illustrated in FIGURE 3-8. Both bouncing and pitching frequencies

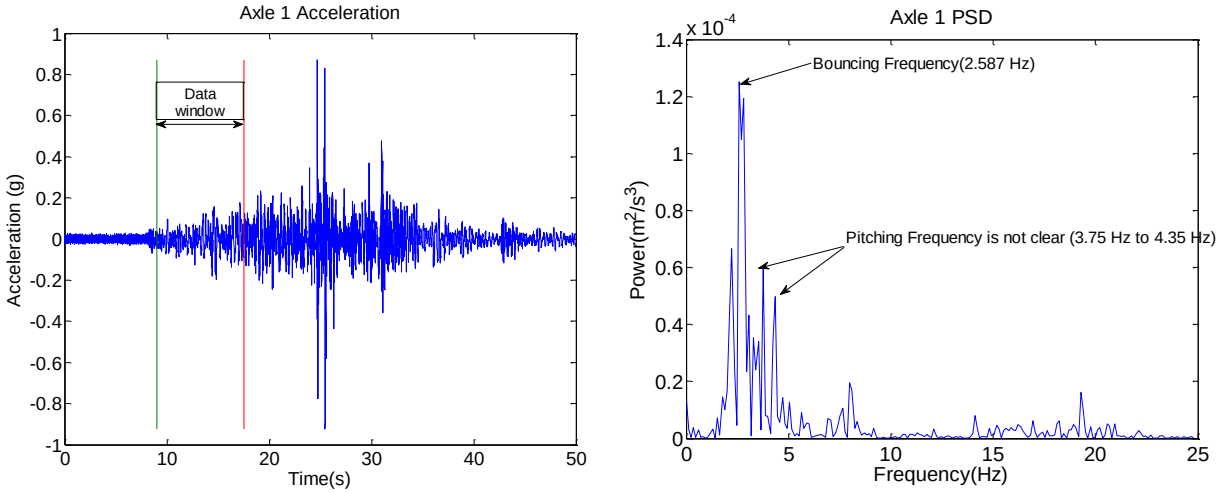

(a) (b)

FIGURE 3-7 Front axle acceleration: (a) axle 1 acceleration; (b) PSD of Axle 1 acceleration

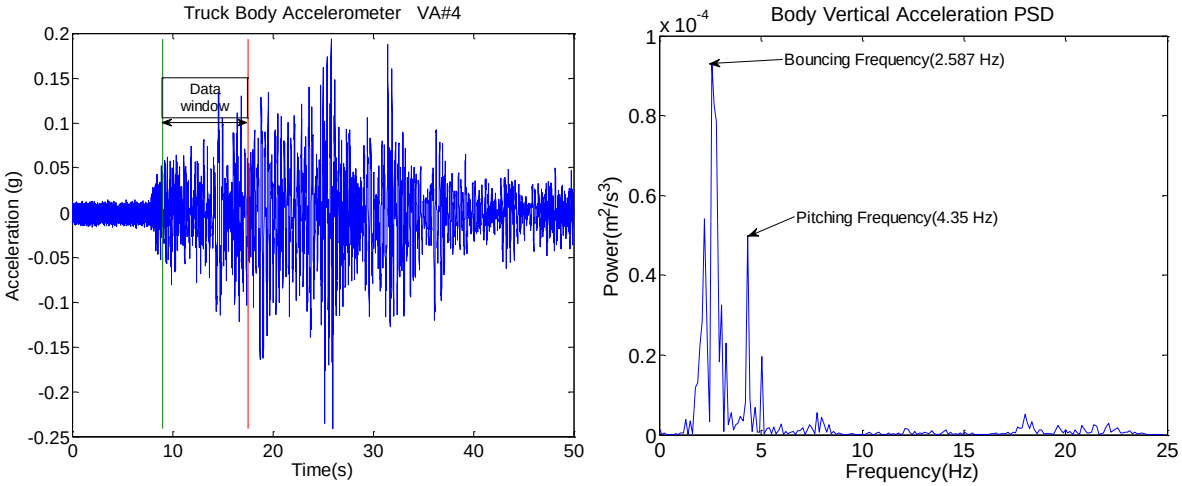

(a) (b)

FIGURE 3-8 Body acceleration: (a) body mass acceleration; (b) PSD of body mass acceleration

are successfully extracted from the graph with 2.587 Hz for bouncing and 4.35 Hz for pitching frequency.

Contrary to the front axle, the pitching angular velocity measured by gyroscope was dominated by the pitching mode of vibration. The pitching motion time history and corresponding frequency spectrum are shown in FIGURE 3-9. The pitching frequency matched the one extracted from the truck body acceleration spectra, while the bouncing frequency was not clearly recognized from these data for the aforementioned reason.

The experiment was repeated for different speeds, and the results are shown in TABLE 3-2. The average bouncing frequency was found as f_b = 2.75 Hz and the average pitching frequency as f_p = 4.22 Hz.

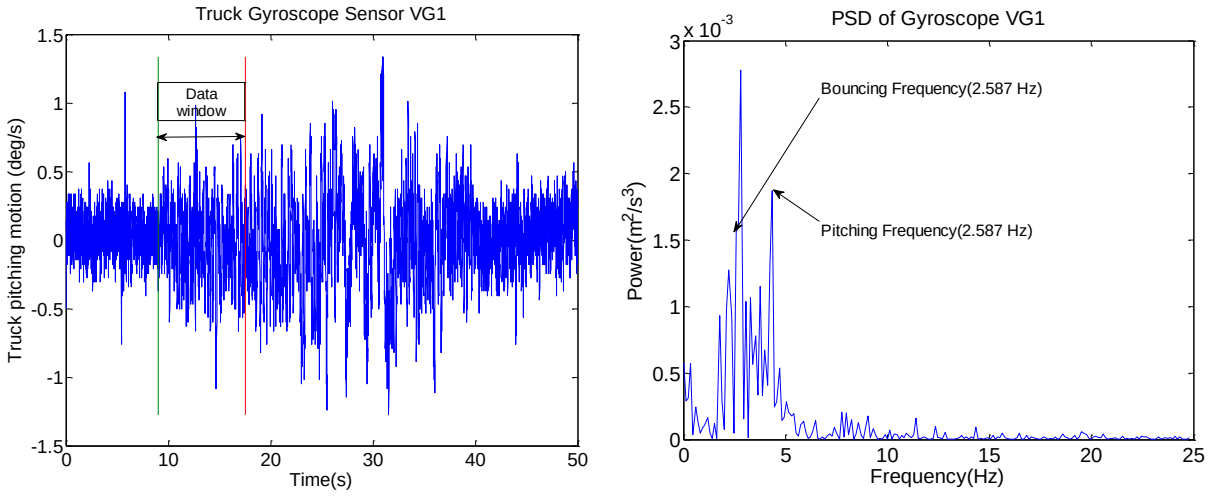

(a) (b)

FIGURE 3-9 Gyroscope: (a) pitching motion time history; (b) PSD of pitching motion

TABLE 3-2 Vehicle bouncing and pitching frequencies from the field test data

Speed	Front Axle Data (Accelerometer VA3)		Body Mass Data (Accelerometer VA4)		Body Mass Pitching (Gyroscope)	
	Bouncing (Hz)	*Pitching (Hz)*	*Bouncing (Hz)*	*Pitching (Hz)*	*Bouncing (Hz)*	*Pitching (Hz)*
27.85 mph	*2.587*	*3.57–4.35*	*2.587*	*4.35*	*2.587–2.7*	*4.35*
33.12 mph	*2.87*	*4.11–4.616*	*2.87*	*4.11–4.616*	*2.87*	*4.11–4.616*
36.26 mph	*2.809*	*4.33*	*2.809*	*4.447*	—	*4.33*
39 mph	*2.778*	*4.227*	*2.778*	*4.106*	*2.778*	*4.227*
39 mph	*2.73*	*4.08*	*2.73*	*4.08*	*2.73*	*4.08*

Going back to FIGURE 3-5, the value of the body mass and moment of inertia are given in TABLE 3-1. The values of k_F and k_R, which refer to the front and rear axles' suspension spring stiffness values, would be chosen to give the same bouncing and pitching frequencies as the measured ones. In this regard, a genetic algorithm (GA) was used to search for stiffness values using the following objective function:

$$E = \begin{Bmatrix} f_b - f_b' \\ f_p - f_p' \end{Bmatrix}^T * \begin{Bmatrix} f_b - f_b' \\ f_p - f_p' \end{Bmatrix} \quad \textbf{3-1}$$

where f_b and f_p were the measured bouncing and pitching frequencies, respectively, and f_b' and f_p' were the calculated bouncing and pitching frequencies of the theoretical half-car model. The GA started the optimization process with $k_F = 2.5\times10^5$ N/m and $k_R = 11\times10^5$ N/m. These values were chosen according to the truck manufacturer's manual [21].

After several iterations, the algorithm archived the objective function with error equal to 4.5×10^{-5} for $k_F = 2.38\times10^5$ N/m and $k_R = 7\times10^5$ N/m. The values of the suspension system were less than the values chosen from the manufacturer's manual. This was either because the truck was loaded, or because the suspension system was wearing out over time.

By running an eigenvalue analysis for the theoretical half-car model using the new spring values, the frequencies were found to be f_b = 2.75 Hz and f_p = 4.22 Hz for bouncing and pitching frequencies, respectively.

To back derive the bridge AP, the vehicle would be modeled as a half-car model with four DOFs for body mass bouncing and pitching rotation, front contact bouncing, and rear contact bouncing (FIGURE 3-10). The body mass m_s and the body inertia I_s were known from the measurements. The contact masses m_F and m_R were insignificant masses used to define the DOFs of the contact points to measure the AP.

The road reaction force on the contact points was calculated using the following equation:

$$\begin{Bmatrix} F_F \\ F_R \end{Bmatrix} = \frac{m_s \ddot{u}_s}{D_1 + D_2} \begin{Bmatrix} D_2 \\ D_1 \end{Bmatrix} + I_s \ddot{\theta}_s \begin{Bmatrix} -\frac{1}{D_1} \\ \frac{1}{D_2} \end{Bmatrix} \qquad \textbf{3-2}$$

The force was then applied to the half-car vehicle model with the four DOFs. The output would be the front and rear contact displacement history, which was the apparent profile.

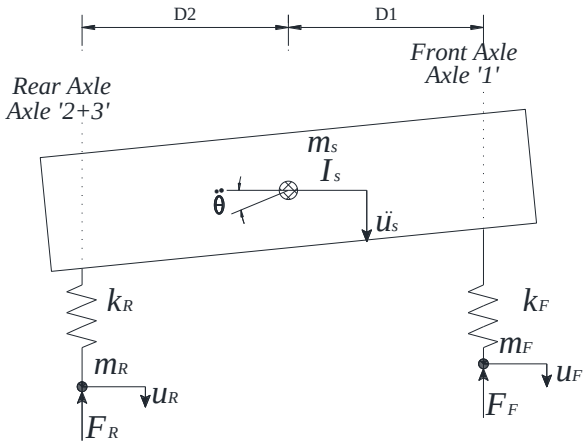

FIGURE 3-10 Half-car model

3.2.3 Field test scenarios

Three scenarios were used to investigate the feasibility of the proposed approach. In Test Scenario #1, the inspection truck crossed the bridge with no public traffic. In Test Scenario #2, a small (public) passenger vehicle crossed the bridge together with the inspection truck. Lastly in Test Scenario #3, a fully loaded truck crossed the bridge together with the inspection truck. The first scenario was repeated three times at 27 mph, 36 mph, and 39 mph driving speeds. The second scenario was repeated two times at 27 mph and 39 mph. Finally, the last scenario was repeated two times at 30 mph and 35 mph; in the first case, the two trucks crossed the bridge with a small time difference, and in the second case the inspection truck crossed the bridge just after the fully loaded truck exited the bridge. FIGURE 3-11 shows photos of all the test cases.

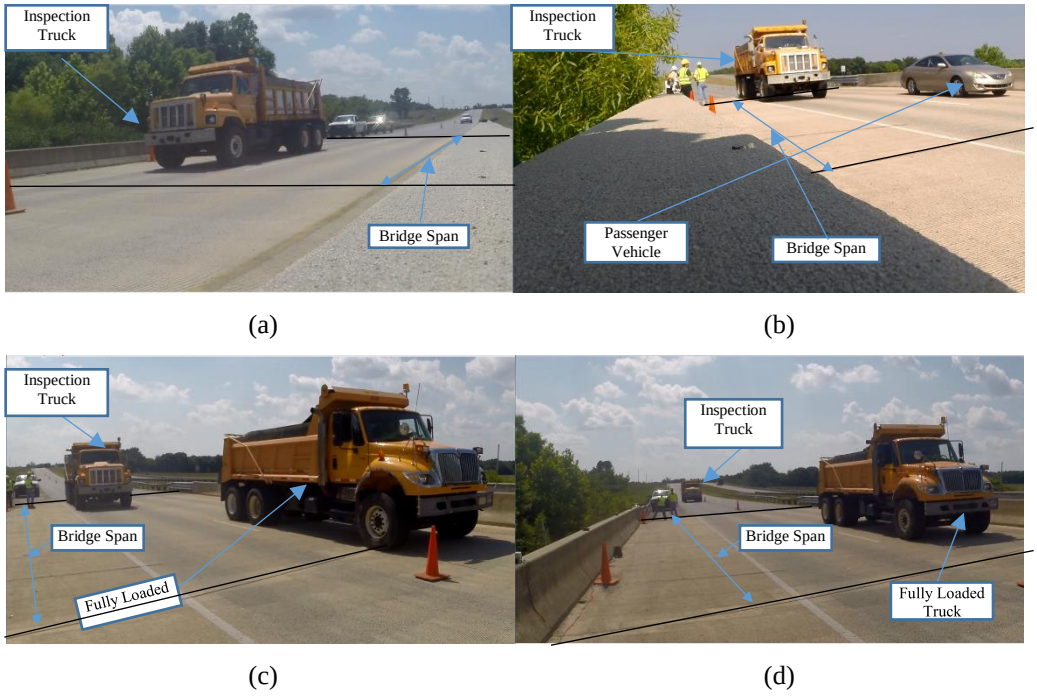

FIGURE 3-11 Field test description: a) Test Scenario #1: only the inspection truck crosses the bridge; b) Test Scenario #2: inspection truck and passenger vehicle cross the bridge together; c) Test Scenario #3: fully loaded truck and inspection truck cross the bridge together; d) Test Scenario #3: inspection truck crosses the bridge after the fully loaded truck crosses the bridge.

3.2.4 Results analysis

The body mass acceleration and the pitching motion recorded from the inspection truck were used as an input to Equation 3-2 to calculate the road reaction forces history of the front and rear axles. The forces were then applied to the theoretical half-car model, and the car equation of motion was solved using the Newmark-beta integration scheme. The solution was applied for the time period starting when the truck entered the bridge until it exited. Since the truck excited in different ways at each run, the initial condition for the truck DOFs would not be the same at the time when the truck entered the bridge. Thus, a linear correction was applied to eliminate the effect of the initial condition as recommended by González,OBrien and McGetrick [15]. The front and rear contact displacement histories would equal the apparent profiles of the front and rear axles (i.e., the bridge displacement under the axle plus the road profile heights). FIGURE 3-12 shows the AP for the front and rear axles for the first testing scenario. The results show that the three runs almost gave the same AP amplitude in Test Scenario #1. Clearly, the rear axles had less perturbations than the front one, due to the high suspension stiffness value for the rear axle. Therefore, it was recommended to use the rear axles' AP for monitoring since it was less influenced by the car excitation. The APs from Test Scenario #1 would be considered as a baseline AP for Test Scenarios #2 and #3.

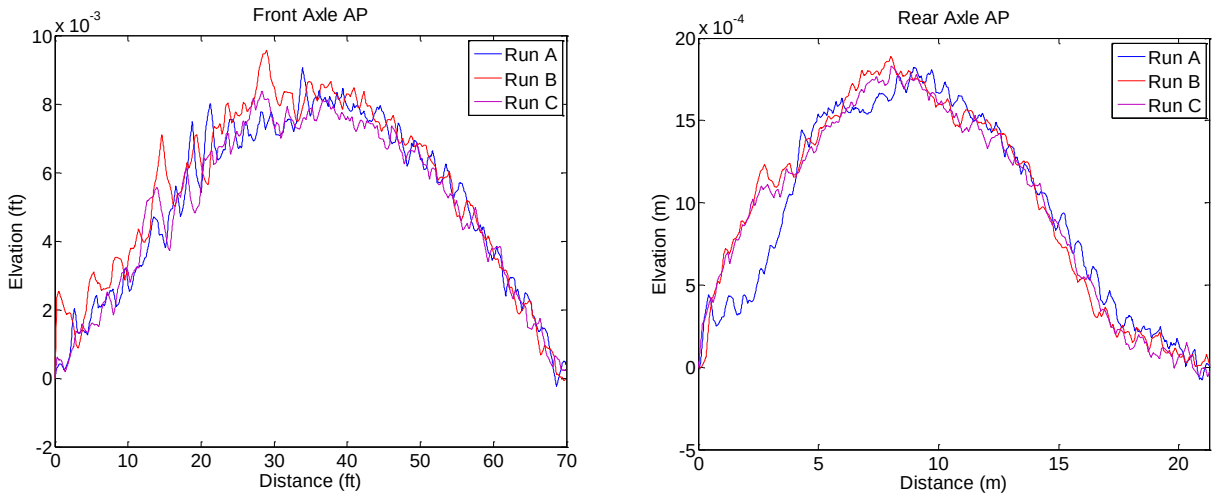

(a) (b)

FIGURE 3-12 AP for Test Scenario #1: (a) front axle AP; (b) rear axle AP

The same process was repeated for Test Scenario #2, where a small passenger vehicle passed with the inspection truck. As shown in FIGURE 3-13, the AP amplitudes reduced for Scenario #2 compared with Scenario #1. This was because the bridge displacement would increase in the second case, and therefore the AP would drop down

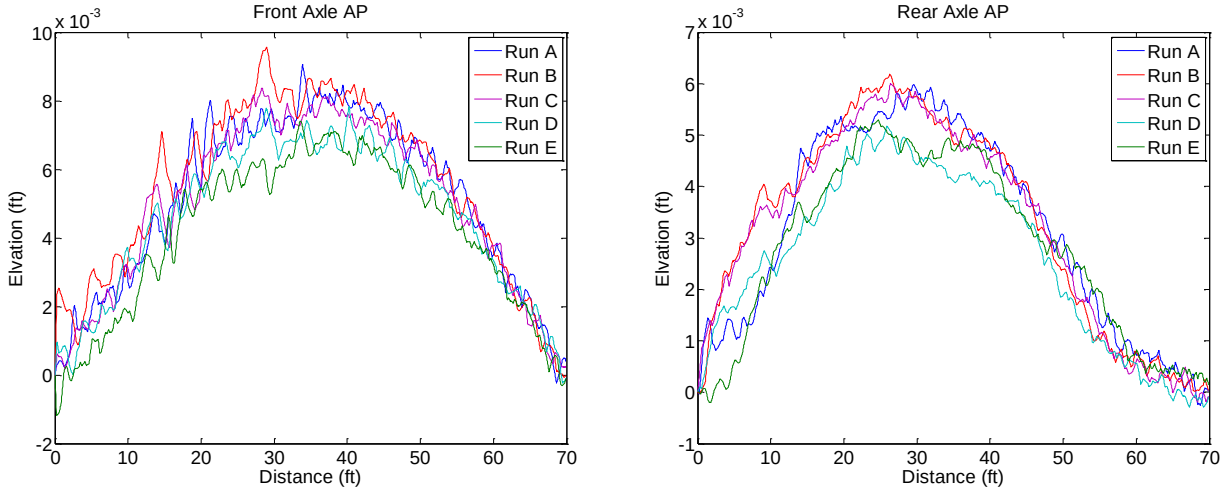

(a) (b)

FIGURE 3-13 AP for Test Scenario #2: (a) front axle AP; (b) rear axle AP

below the baseline AP. Herein, the rear axle showed better observation than the front axle for the same reason discussed before.

For Test Scenario #3, the same procedure was repeated to calculate the bridge AP. For the first case, the two trucks arrived at the bridge at almost the same time. This would induce a high level of deformation to the bridge, which should be directly reflected on the AP. The AP for the first case is shown in FIGURE 3-14. As expected, the AP amplitude shows a drastic drop compared to the baseline AP in Scenario #1. This observation was found for both the front and rear axles. In contrast, for the second case, the AP showed to be similar to the baseline AP, since the inspection truck passed the bridge after the fully loaded truck left the bridge. This indicates that the algorithm was not influenced by the vibration status of the bridge; in other words, the forward traffic does not affect the algorithm sensitivity.

To get the BDPDs, the baseline AP was chosen from Test Scenario #1, and the BDPDs for Test Scenarios #2 and #3 were calculated by subtracting the APs from the

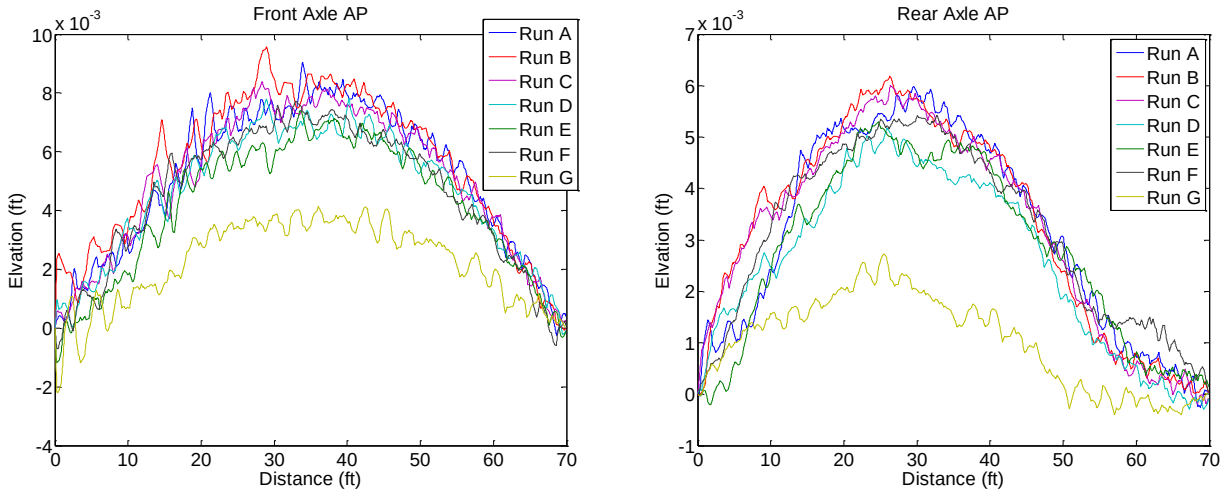

(a) (b)

FIGURE 3-14 AP for Test Scenario #3: (a) front axle AP; (b) rear axle AP

baseline AP. The results are shown in FIGURE 3-15. The BDPDs show a clearer difference for each test scenario, while the rear axles still show less perturbations than the front axle. The effect of additional traffic is obvious in the figure, which indicates the algorithm's feasibility in identifying the changes in the bridge displacement.

The previous results show that the algorithm successfully detects the change in the bridge displacement due to additional traffic. Therefore, the same concept can be applied to detect the increase in the bridge displacement due to structural damage. In this case, the inspection truck would cross the bridge to back derive the baseline AP. Then after 2 years of mandated interval, the same inspection truck would cross the bridge again. If the back-calculated AP reduced from the baseline AP, this would indicate that there was an increase in the bridge displacement that may be related to a degradation in the bridge structure integrity. In this way the approach could be used to provide a fast screening for the bridges on the transportation network to quantify the bridges that require immediate maintenance. To reiterate, the approach uses only measurements from the inspection truck, which makes the approach very cost-effective compared to traditional monitoring techniques.

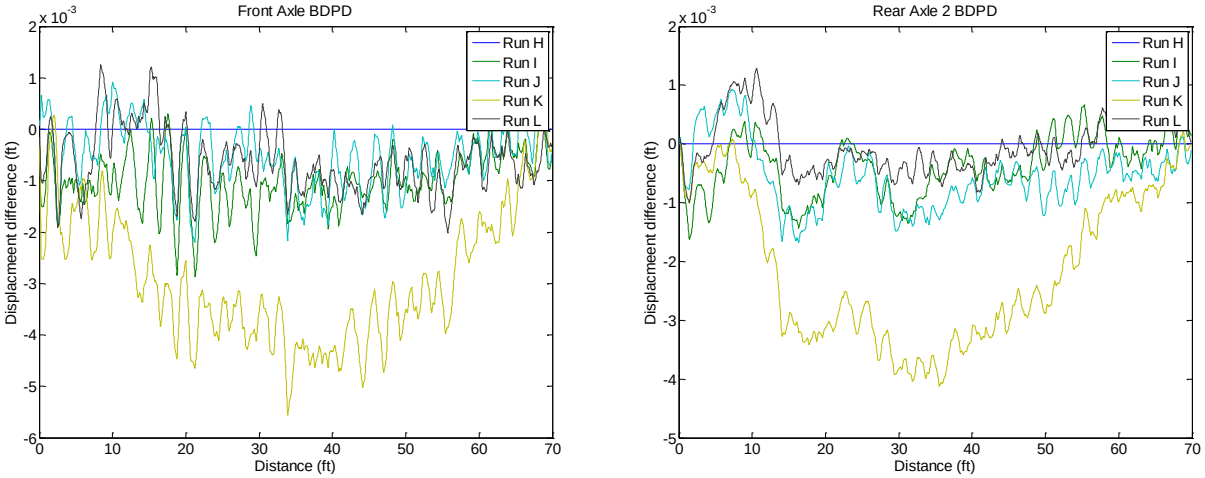

(a) (b)

FIGURE 3-15 BDPDs for Test Scenario #2 and #3: (a) front axle BDPDs; (b) rear axle BDPDs

3.3 Summary

This chapter introduced the road reaction method as a novel approach for monitoring bridges' structural health condition. The approach was investigated for the testbed bridge using an instrumented truck. First, an equivalent theoretical truck model was built for the truck using the field measurements. The truck was modeled as a theoretical half-car model with two DOFs accounting for body bouncing and pitching rotation. The truck mass and mass moment of inertia were calculated using axle weights. The suspension stiffness values were initially selected based on the manufacturer's manual. Using a GA optimization algorithm, the values were changed to match the measured bouncing and pitching frequencies. The road reaction forces were calculated, and then the forces were applied to the calibrated theoretical half-car model. The model equation-of-motion was then solved using the Newmark-beta integration scheme. A linear correction was applied to eliminate the effect of the truck initial condition of the solution. The results show that the algorithm successfully detected the changes in the bridge displacement due to the presence of additional traffic on the bridge. The same approach could be applied to detect the changes in the bridge displacement due to structural damage, which could be used for monitoring the bridge degradation with time. The approach uses only measurements from the inspection truck, which makes it very economical compared to traditional health monitoring techniques.

4 Ultrasonic Measurement for Cracks

This chapter presents a wireless sensing system that has been developed for its field deployment, being integrated in two different ultrasonic nondestructive evaluation techniques for detecting/measuring cracks: (1) the diffuse ultrasonic technique for measuring depths of cracks in concrete and (2) a technique for detecting small cracks in metallic specimens. Section 4.1 describes the developed hardware, including an ultrasonic board and a battery-powered pulser board. Section 4.2 summarizes the results from two ultrasonic tests, including a dynamic crack monitoring in an aluminum dog-bone specimen and a diffuse ultrasonic test of a crack in a concrete specimen.

4.1 Development of ultrasonic measurement setups based on wireless sensing system

As a widely used technique, ultrasonic NDE can be applied to monitor crack growth in materials. An ultrasonic board was developed to work in combination with the *Martlet* wireless sensing system [22]. FIGURE 4-1 shows the details of the ultrasonic board, which can provide excitation signals to an ultrasonic transmitting transducer and receive signals from a receiving transducer, with the capability of onboard signal conditioning.

In addition, a battery-powered pulser was developed to realize a high-voltage pulse excitation to the transmitting transducer for concrete applications. FIGURE 4-2 shows the functional diagram of the pulser and the latest version of the pulser board. The pulser is powered by 18V DC power. The input trigger to the pulser is a series of 3.3V square waves from a *Martlet* wireless unit with a programmable repetition rate, and the output is a series

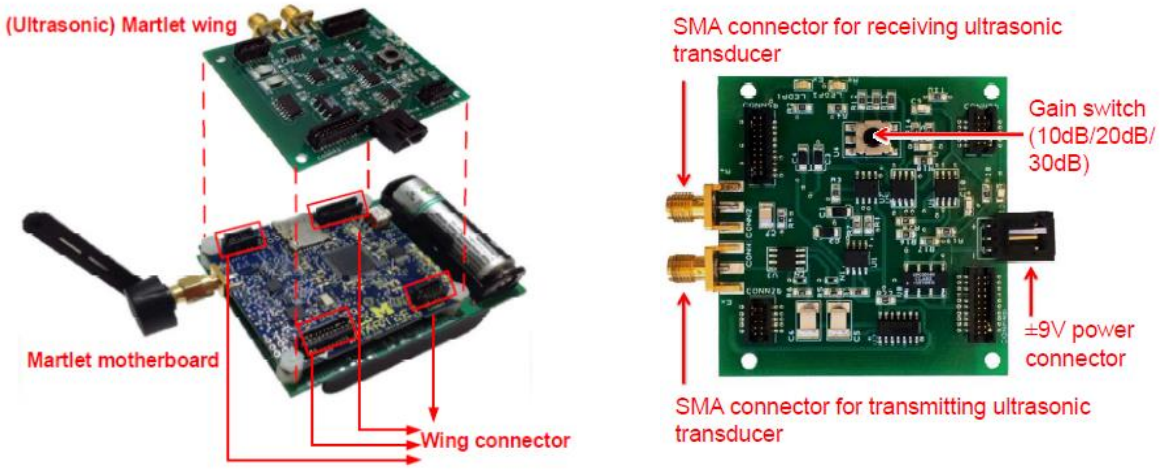

(a) (b)

FIGURE 4-1 Ultrasonic wireless sensing unit: (a) ultrasonic board and a *Martlet* wireless unit; (b) close-up view of the ultrasonic board

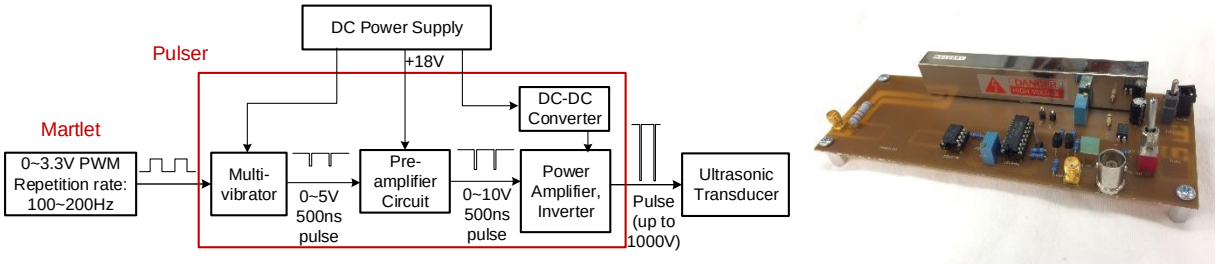

(a) (b)

FIGURE 4-2 Battery-powered pulser board: (a) functional diagram; (b) photo

of short pulses with a magnitude adjustable up to 1000V. The pulse width is also adjustable from 200 ns to 1 μs using an on-board potentiometer.

4.2 Experimental validation

To validate the performance of the wireless ultrasonic NDE, two different ultrasonic tests were carried out. Subsection 4.2.1 describes an ultrasonic test of a crack in open–close motion. Subsection 4.2.2 describes a diffuse ultrasonic test of a crack on a concrete specimen.

4.2.1 Measurement of a breathing crack in a metallic specimen

A breathing crack is one that opens and closes due to dynamic excitations. The ultrasonic measurement was conducted for a breathing crack on an aluminum dog-bone specimen that was excited by a modal shaker to force the crack into close-and-open cycles. Note that this simulated the ultrasonic detection of cracks in steel bridge components that are in open–close vibrational motion caused by passing-by traffic. FIGURE 4-3(a) shows the dimension of the specimen and the sensor layout. The center line of the two 500 kHz ultrasonic transducers (Ultran Group WC50-0.5) was located across the crack tip initiated in a prior test (FIGURE 4-3(b)). Strain gages were attached at the bottom of the specimen to measure the longitudinal deformation of the specimen during the test. Test setup details are shown in FIGURE 4-4(a). Two accelerometers (one for a cabled system and one for a wireless system) were attached to the specimen to measure vertical acceleration. The wireless sensing unit used in this test included an ultrasonic wing board, a strain gage wing

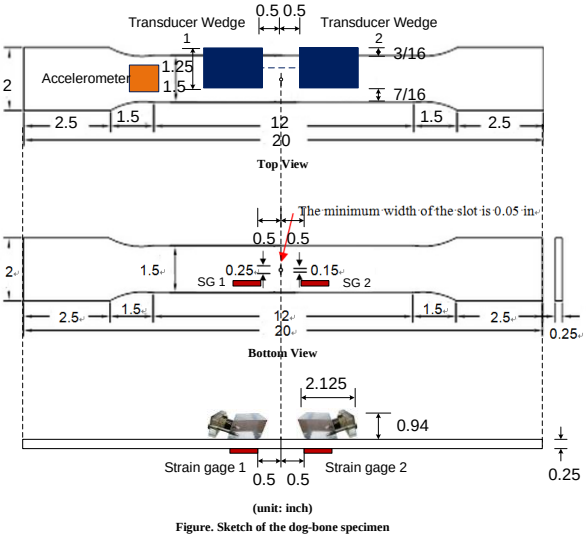

(a)

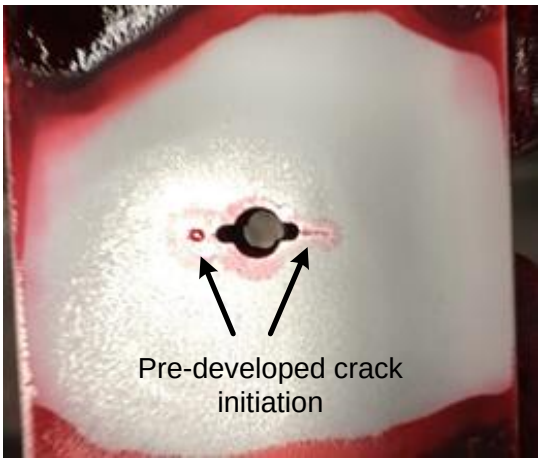

(b)

FIGURE 4-3 Ultrasonic dynamic test: (a) specimen dimension and sensor layout; (b) pre-developed crack initiation

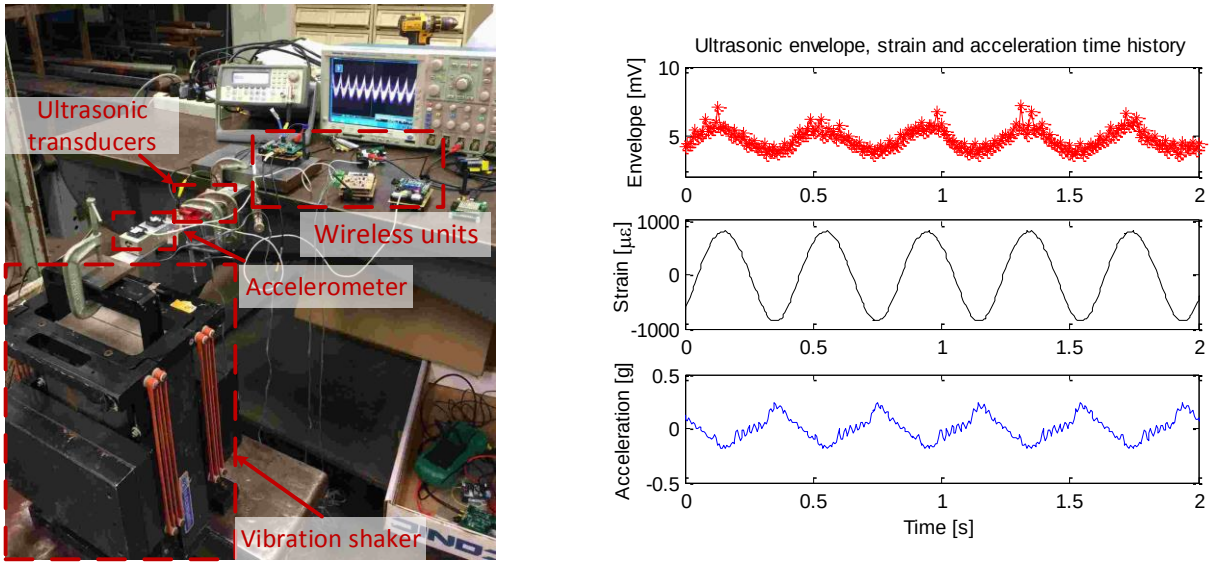

(a) (b)

FIGURE 4-4 Test results: (a) test setup; (b) sensor data plots

board, and an acceleration wing board, which were all connected to a *Martlet* wireless unit. The test results for a sinusoidal excitation at frequency 2.5 Hz are summarized in FIGURE 4-4(b). The ultrasonic envelope signal shows a sinusoidal waveform the same as the shaker vibration waveform, which confirms the open–close breathing motion of the crack.

4.2.2 Crack detection on concrete specimen with wireless sensing system

The ultrasonic pulser board was tested with a *Martlet* wireless unit on a concrete specimen. FIGURE 4-5 shows the test setup, involving two test scenarios. In the first scenario, the two ultrasonic transducers (Ultran Group WC50-0.5 and GC500-D13) were placed on top of the concrete surface without a crack. In the second scenario, the two ultrasonic transducers were placed across a crack. An 18V DC power supply was used to power the pulser. The pulse magnitude was set around 900V and the pulse width at 800 ns. The *Martlet* wireless unit was used to generate a 0~3.3V square wave trigger signal to the

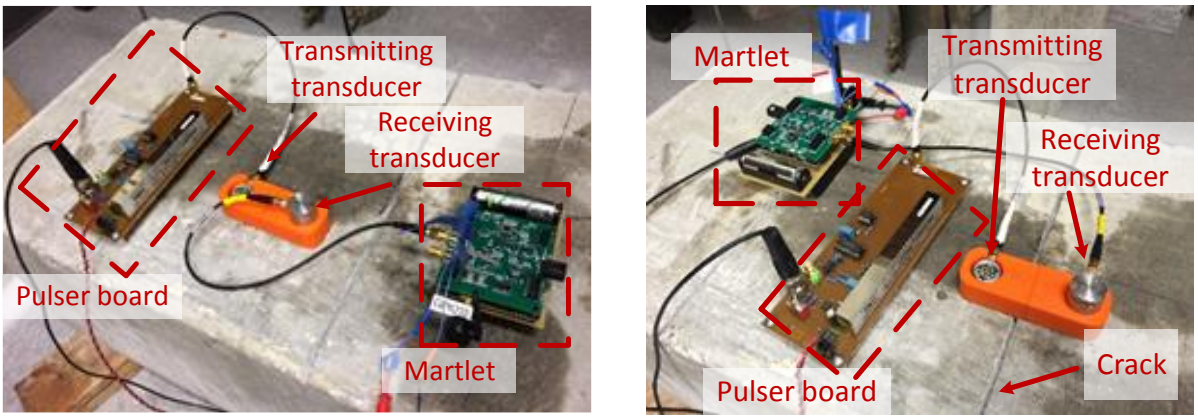

(a) (b)

FIGURE 4-5 Ultrasonic concrete crack test (wireless system): (a) without crack; (b) with crack

pulser with a repetition rate of 100 Hz. The performance of the wireless sensing system was compared to the cabled receiver results when both were using the battery-powered pulser. The sampling frequency of the wireless system was 2 MHz, and the sampling frequency of the cabled receiver was 50 MHz. The amplification gain was set to be 30 dB for both systems.

FIGURE 4-6 shows the comparison results between the wireless system and the cabled receiver for both test scenarios (without and with a crack). In each scenario, the waveform obtained from the wireless system was comparable to those obtained by the cabled receiver. The results also showed that the magnitude of the waveform decreases when a crack exists.

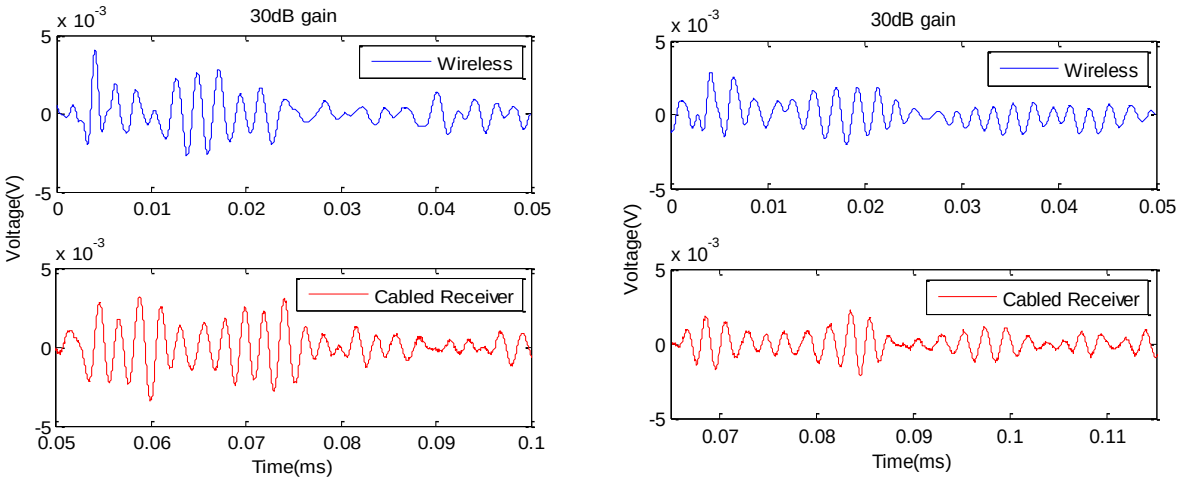

(a) **(b)**

FIGURE 4-6 Ultrasonic concrete crack test results: (a) without crack; (b) with crack

4.3 Summary

In this research, an ultrasonic NDE device combined with a wireless sensing technique was developed. The development features an ultrasonic wing board for the *Martlet* wireless unit and a battery-powered high-voltage pulser board. The wireless ultrasonic device was tested on an aluminum specimen and a concrete specimen for crack detection. The test results indicate the capability of the *Martlet* wireless sensing system for monitoring crack growth in both metallic and concrete materials.

5 Conclusions and Recommendations

In conclusion, this report first introduced the testbed highway bridge and the *Martlet* wireless sensing system in Chapter 1. The validation tests demonstrated the reliability and versatility of the *Martlet* system. In addition, by utilizing the modal properties obtained from the acceleration response collected by *Martlet*, an accurate finite element model of the testbed highway bridge is achieved for later bridge weigh-in-motion and drive-by inspection analysis.

In Chapter 2, the moving force identification algorithm is presented to detect the axles and total weight of vehicles driving through the bridge. In most cases, the presented algorithm can achieve accurate identification results, including the most challenging case with two heavy trucks driving through the bridge at the same time. Although initially the weight of the second truck couldn't be estimated accurately, the accuracy significantly improved after the dynamic influence line was improved.

Chapter 3 introduced the road reaction method as a novel approach for monitoring a bridge's structural health condition. The approach was investigated for the testbed bridge using an instrumented truck. The results show that the algorithm successfully detected the changes in the bridge displacement due to the presence of additional traffic on the bridge. It is expected the same approach could be applied to detect the changes in the bridge displacement due to structural damage, which could be used for monitoring the bridge degradation with time. Considering that the approach uses only measurements from the inspection truck, it makes the inspection approach very economical compared to traditional health monitoring techniques.

Finally, in Chapter 4, an ultrasonic NDE device incorporated with wireless sensing technique was introduced. The wireless ultrasonic device was tested on an aluminum specimen and a concrete specimen for crack detection. The test results indicate the capability of the *Martlet* wireless sensing system for monitoring crack growth in both metallic and concrete materials.

In the future, the team plans to utilize the *Martlet* wireless sensing system in more field experiments to assess the reliability of its performance. Furthermore, the *Martlet* wireless sensing system will be developed for long-time structural health monitoring purpose, in addition to short-term tests in this project. The low-power consumption mode and solar power charging features will be developed to allow the wireless sensing system operate on the structure for months or years when needed. The developed bridge weigh-in-motion algorithms will also be validated by more field experiments.

6 References

[1] Kane, M., Zhu, D., Hirose, M., Dong, X., Winter, B., Häckell, M., Lynch, J. P., Wang, Y. and Swartz, A., Development of an extensible dual-core wireless sensing node for cyber-physical systems, *Proceedings of SPIE, Nondestructive Characterization for Composite Materials, Aerospace Engineering, Civil Infrastructure, and Homeland Security*, San Diego, California, USA, (2014).

[2] Cooklev, T., *Wireless Communication Standards : a Study of IEEE 802.11, 802.15, and 802.16*, Standards Information Network IEEE Press New York (2004).

[3] Dong, X., Zhu, D., Wang, Y., Lynch, J. P. and Swartz, R. A., Design and validation of acceleration measurement using the Martlet wireless sensing system, *Proceedings of the ASME 2014 Smart Materials, Adaptive Structures and Intelligent Systems (SMASIS)*, Newport, RI, (2014).

[4] Juang, J. N. and Pappa, R. S., An eigensystem realization algorithm for modal parameter identification and modal reduction, *Journal of Guidance Control and Dynamics*, 8(5), 620-627 (1985).

[5] Rowley, C. W., *Moving force identification of axle forces on bridges*, University College Dublin (2007).

[6] O'Brien, E. J., Quilligan, M. and Karoumi, R., Calculating an influence line from direct measurements, (2006).

[7] Zhao, H., Uddin, N., O'Brien, E. J., Shao, X. and Zhu, P., Identification of vehicular axle weights with a bridge weigh-in-motion system considering transverse distribution of wheel loads, *Journal of Bridge Engineering*, 19(3), 04013008 (2013).

[8] Davis, S. L., Goldberg, D., DeGood, K., Donohue, N. and Corless, J., The Fix We're In For: The State of Our Nation's Bridges 2013, (2013).

[9] Chupanit, P. and Phromsorn, C., The importance of bridge health monitoring, *International Science Index*, 6, 135-138 (2012).

[10] Kim, C. W. and Kawatani, M., Challenge for a drive-by bridge inspection, *International Conference; 10th, Structural safety and reliability; Safety, reliability and risk of structures, infrastructures and engineering systems; ICOSSAR2009; Osaka, Japan*, (2009).

[11] Yang, Y. and Lin, C., Vehicle–bridge interaction dynamics and potential applications, *Journal of sound and vibration*, 284(1), 205-226 (2005).

[12] Yang, Y.-B., Lin, C. and Yau, J., Extracting bridge frequencies from the dynamic response of a passing vehicle, *Journal of Sound and Vibration*, 272(3), 471-493 (2004).

[13] Lin, C. and Yang, Y., Use of a passing vehicle to scan the fundamental bridge frequencies: An experimental verification, *Engineering Structures*, 27(13), 1865-1878 (2005).

[14] McGetrick, P. J., Gonzlez, A. and OBrien, E. J., Theoretical investigation of the use of a moving vehicle to identify bridge dynamic parameters, *Insight-Non-Destructive Testing and Condition Monitoring*, 51(8), 433-438 (2009).

[15] González, A., OBrien, E. J. and McGetrick, P., Detection of bridge dynamic parameters using an instrumented vehicle.

[16] McGetrick, P., González, A. and O'Brien, E. J., Monitoring bridge dynamic behaviour using an instrumented two axle vehicle.

[17] González, A., OBrien, E. J. and McGetrick, P., Identification of damping in a bridge using a moving instrumented vehicle, *Journal of Sound and Vibration*, 331(18), 4115-4131 (2012).
[18] Keenahan, J., OBrien, E. J., McGetrick, P. J. and Gonzalez, A., The use of a dynamic truck-trailer drive-by system to monitor bridge damping, *Structural Health Monitoring*, 1475921713513974 (2013).
[19] Malekjafarian, A., McGetrick, P. J. and OBrien, E. J., A review of indirect bridge monitoring using passing vehicles, *Shock and Vibration*, (2015).
[20] OBrien, E. J. and Keenahan, J., Drive‐by damage detection in bridges using the apparent profile, *Structural Control and Health Monitoring*, 22(5), 813-825 (2015).
[21] NAVISTAR, HX™ SERIES SERIES BODY BUILDER, (2016).
[22] Dong, X., Chen, S., Zhu, D., Kane, M., Wang, Y. and Lynch, J. P., High-speed heterogeneous data acquisition using Martlet - a next-generation wireless sensing device, *Proceedings of the Sixth World Conference on Structural Control and Monitoring (6WCSCM)*, Barcelona, Spain, (2014).